The structure and origin of nodular chromite from the Troodos ophiolite, Cyprus, revealed using high-resolution X-ray computed tomography and Electron Backscatter Diffraction

H. M. Prichard[a], S. J. Barnes[b] , B. Godel [b], S. M. Reddy[c] , Z. Vukmanovic[c], A. Halfpenny[d] , C. R. Neary[a] and P. C. Fisher[a]

a School of Earth and Ocean Sciences, Cardiff University, Cardiff, CF10 3AT, Wales, UK.
b CSIRO Earth Science and Resource Engineering, ARRC, 26 Dick Perry Avenue, Kensington, WA, 6151, Australia.
c Dept. Of Applied Geology, Curtin University, Kent St., Bentley, WA 6102, Australia
d Electron Microscopy Facility, Department of Imaging and Applied Physics, Curtain University, GPO Box U1987, Perth, WA 6845, Australia.

Prichard@cardiff.ac.uk corresponding author 0044 2920484731

Key words Chromite, nodule, skeletal crystal, hopper crystal.

Abstract

Nodular chromite is a characteristic feature of ophiolitic podiform chromitite and there has been much debate about how it forms. Nodular chromite from the Troodos ophiolite in Cyprus is unusual in that it contains skeletal crystals enclosed within the centres of the nodules and interstitial to them. 3D imaging and electron backscatter diffraction have shown that the skeletal crystals within the nodules are single crystals that are surrounded by a rim of polycrystalline chromite. 3D analysis reveals that the skeletal crystals are partially or completely formed cage or hopper structures elongated along the <111> axis. The rim is composed of a patchwork of chromite grains that are truncated on the outer edge of the rim. The skeletal crystals formed first from a magma supersaturated in chromite and silicate minerals crystallised from melt trapped between the chromite skeletal crystal blades as they grew. The formation of skeletal crystals was followed by a crystallisation event which formed a silicate-poor rim of chromite grains around the skeletal crystals. These crystals show a weak preferred orientation related to the orientation of the core skeletal crystal implying that they formed by nucleation and growth on this core, and did not form

by random mechanical aggregation. Patches of equilibrium adcumulate textures within the rim attest to in situ development of such textures. The nodules were subsequently exposed to chromite undersaturated magma resulting in dissolution, recorded by truncated grain boundaries in the rim and a smooth outer surface to the nodule. None of these stages of formation require a turbulent magma. Lastly the nodules impinged on each other causing local deformation at points of contact.

1. Introduction

Fossilised oceanic crust or ophiolite complexes often contain podiform chromitite. These are bodies of massive high chromium chromite that are commonly economically viable orebodies, as in Kazakhstan (e.g. Melcher et al., 1997). Podiform chromitites are located within mantle harzburgite surrounded by a lens of dunite and are often found in the transition zone between the mantle and overlying crustal dunite, as well as in the dunite itself (Pagé et al., 2009; Roberts and Neary, 1993; Prichard and Neary, 1982; Thayer, 1964; Uysal, 2005; González-Jiménez et al., 2014). Much of a typical podiform chromitite is composed of massive granular chromite, but the pods are also often made up of stacks of discontinuous layers of chromitite. Nodular and orbicular chromite are common components of podiform chromitite in many ophiolites of all ages and have been described by many authors (Fig. 1), e.g. from California (Ryerson and Smith 1940), Cuba (Thayer, 1964), Oman (Brown, 1980), Pakistan (Ahmed, 1982), Turkey (Paktunc, 1989), northern China (Huang et al., 2004) and southern Tibet (Xu et al., 2011).

The origin of nodular chromite is controversial as is the origin of podiform chromitite. Nodular and orbicular chromite, although not the major forms of chromite in podiform chromitite, provide important clues to the mode of formation of this style of deposit. In this contribution, we provide new microtextural information on a rare variety of nodular chromite associated with skeletal chromite that provides a unique insight into the contentious question of how chromite nodules crystallise.

Figure 1 here.

Nodular chromite is restricted to ophiolitic chromitite and is absent from stratiform chromitite in layered intrusions (Matveev and Ballhaus, 2002), such as the Bushveld complex in South Africa, (e.g Irvine, 1977; Jackson, 1968; Naldrett, 2009). The restriction of the occurrence of nodular chromite to ophiolite complexes indicates a formation mechanism that is unique to an oceanic setting.

Nodules of chromite range from 2-30 mm in size and are approximately spherical or ovoid in shape. They can however have flat surfaces giving the nodules distinctive cubic shapes with rounded corners (Ceuleneer and Nicholas, 1985). The nodules usually have fairly smooth outer surfaces and are mostly composed of chromite. They are commonly associated with euhedral chromite grains, as first described by Thayer (1969). Nodules generally occur in groups, often in layers and may be in contact with each other (Ahmed, 1982) sometimes appearing to have collided with each other causing deformation of the nodules (e.g. Paktunc, 1990; Prichard and Neary, 1982). Nodular ore types are typically restricted to the peripheries of the ore bodies or to smallish ore bodies, usually they occur in close proximity to the dunite halo (Ballhaus pers. comme).

Chromite in some cases forms rims around cores of silicates producing orbicular chromite or chromite anti-nodules (Brown, 1980). Multiple thin shells of alternating chromite and olivine form more complex orbicular chromite (Ahmed, 1982; Dickey, 1975; Greenbaum, 1977; Huang et al., 2004; Melcher, 1977; Thayer, 1969; Zhou et al., 2001).

There is no agreement on how these nodules form or even whether the nodules crystallised inwards towards the core or grew from the centre outwards. Nodules have been reported to lack chemical

zoning (Ahmed, 1982; Greenbaum, 1977). Other researchers report chemical differences towards the rim including Cr decrease and Ti increase (Leblanc and Ceuleneer, 1992).

In rare cases the nodules can have skeletal chromite in their cores. Examples include the samples from the Troodos ophiolite complex presented in this study and by Greenbaum (1977). Skeletal chromite has also been reported from the Vourinos ophiolite complex in Greece (Christiansen and Olesen, 1990) and the Zunhua ophiolite in northern China (Huang et al., 2004). Skeletal chromite has also been described from komatiites (e.g. Godel et al., 2013) from spinifex-textured flow tops and coarse grained olivine cumulates and also within massive sulphide ores at the contact with overlying komatiite flows (Dowling et al., 2004; Groves et al., 1977). However, these skeletal grains lack the distinctive association with nodules reported here. Skeletal chromite has been interpreted as the result of rapid crystal growth from chromite-supersaturated magma (Godel et al., 2013). This is also the process suggested by Greenbaum (1977) for the formation of the nodules associated with skeletal forms from Cyprus.

1.1 Hypotheses for the origin of nodular and orbicular chromite

There have been many mechanisms suggested for the growth of nodular and orbicular chromite. The main theories include:

(1) Growth from suspended aggregates of chromite accumulating concentrically in fast flowing magma (Huang et al., 2004) with aggregation, and coalescence or clustering of free-formed chromite grains prior to settling (Ahmed, 1982; Lago et al., 1982; Lorand and Ceuleneer, 1989; Thayer, 1969) and similarly snowballing in a turbulent flow as suggested by Dickey (1975).

(2) Separation from already consolidated chromite ore and abrasion during rock flowage (van der Kaaden, 1970).

(3) Collection of chromite from silicate magma during magma mingling by its attachment to a water-rich fluid that forms an envelope around the chromite producing spherical aggregates (Ballhaus, 1998; Matveev and Ballhaus, 2002).

(4) Formation in turbulent picritic magma flow accompanied by a water-rich fluid (Moghadam et al., 2009).

(5) Solidification of globules from a (hypothetical) chromite-rich immiscible liquid (Pavlov, 1977).

(6) Association with silica-rich droplets arising from wall-rock reaction causing chromite crystallisation around the droplet and their 'collapse' to form chromite nodules (Zhou et al., 2001). This builds on the ideas of magma processes in oceanic mantle developed by Keleman (1995).

Figure 2 here

1.2 Sample locations

This paper presents results of a study of a suite of samples from the Troodos Ophiolite. The Troodos Mountains in Cyprus host the classic ophiolite sequence exposed on Mt Olympus : mantle harzburgite is surrounded and overlain by dunite, wehrlite and pyroxenite that are in turn overlain by gabbro. The whole sequence is truncated and dissected into blocks by faulting. Podiform chromitite is situated mainly at the harzburgite/dunite junction and occurs as discontinuous layers that occasionally were large enough to be economically extractable. The largest concentrations of chromitite were at Kokkinorotsos mine, from which at least 0.5 million tons of chromitite have been extracted (Greenbaum, 1977) (Fig.2). The chromite nodules studied here are from two localities just west of Kokkinorotsos on Mt Olympus, (chromite occurrences 2 and 3, Fig. 2) where the best orbicular, nodular and skeletal chromites were first described by Greenbaum (1977) and

140 further studied by Leblanc (1980).

141

142 **2. Methods**

143

144 Two samples of nodular chromite containing skeletal chromites were selected for 3D imaging.
145 Cores of 25 mm diameter were drilled into the nodular chromite. These cores were scanned using
146 the XRADIA XRM 500 high-resolution 3D X-ray microscope system at the Australian Resources
147 Research Centre (ARRC, Kensington, Western Australia). The scanner was set-up to 160 kvV
148 voltage, 10 W power and a voxel size of 13 µm. A total of 2000 projections were recorded over
149 360° for each sample and were used to reconstruct the 3-D volumes. The generated data were
150 processed and analysed using AvizoFire® and CSIRO-developed codes, following methods
151 described by Godel (2013). One core was subsequently cut and polished down to a particular slice
152 where the geometric centre of a skeletal crystal-cored nodule had been located in the 3D scan. This
153 area was selected for electron backscatter diffraction (EBSD) analysis. The sample surface was
154 prepared for EBSD via chemical-mechanical polishing (CMP) using colloidal silica (Prior et al.
155 1999, Halfpenny, 2010; Halfpenny et al., 2013) and given a thin carbon coat to prevent charging in
156 the SEM. EBSD data were collected from two systems. Large area simultaneous EBSD and EDS
157 mapping of a single nodule was undertaken using Tescan Mira3 field emission SEM, housed in the
158 Electron Microscopy Facility at Curtin University, Perth, using an accelerating voltage of 20kV and
159 probe current of 17nA. EBSD data were collected by a NordlysNano EBSD detector, whilst EDS
160 data were collected on a X-Max 150 silicon drift detector. Data were acquired using the automatic
161 mapping capability of Oxford AZtec 2.2 Full crystallographic orientation data from individual
162 chromite grains were obtained also from automatically indexed Kikuchi diffraction patterns
163 collected using a Bruker e$^-$flash detector fitted on a Zeiss Ultraplus FEG SEM at the CSIRO
164 facilities, Kensington, Western Australia. Coincident energy dispersive X-ray spectra (EDS) were
165 collected with a Bruker XFlash 5030 silicon drift EDS detector and this information was used to

accurately separate the phases. This SEM was operated using an accelerating voltage of 20kV, a 120µm aperture, in high current mode which produced a beam current of 12.1nA. The EBSD data were collected using the Bruker Quantax Espirit 1.9 software, using a resolution of 200x150 pixels, a 11.5ms exposure time and a step size of 5.12µm (determined by the size of the smallest grain of interest). All EBSD data were post-processed using Oxford Instruments Channel 5 software to remove mis-indexed points and interpolate non-indexed points (Prior et al., 2009). The corrected data files were then used to generate the presented EBSD images. Chromite analyses were performed using a Cambridge Instruments (ZEISS NTS) S360 scanning electron microscope (SEM), coupled to an Oxford Instruments INCA energy plus which included both an energy dispersive (ED) and a wave dispersive (WD) X-ray analytical system at Cardiff University. Chromite single point analyses were performed also with a 20kV accelerating voltage, 20 nA beam current and fixed beam size (approximately 10-15 nm) with a live-time of 50 s for ED. A cobalt standard and separate chromite standard were used to monitor for instrumental drift. X-ray fluorescence mapping was carried out using a Bruker Tornado desktop X-ray microscope at CSIRO, Perth, equipped with silicon drift detector operating at count rates of about 100-150 kcps, x-ray tube conditions 50 kV, 600 microamps, spot size 25 microns, 25 micron step size, x-ray energy resolution less than 145 eV. Results were ZAF corrected and presented as element concentration maps using native Bruker software.

3. Results

3.1 Nodules and skeletal crystals in 2D

Samples were collected from locality 2 (Fig. 2) where there are dunites containing nodular and skeletal chromite. Layers of nodules contain skeletal chromite growths both in their cores and between nodules. The skeletal crystals are particularly common at the edges of the layers of nodules

192 (Figs. 3A, and 4) and there are more skeletal chromites in the adjacent dunite (Fig. 3A).

193

194 Figure 3 here

195

196 The nodules are approximately 1 cm in diameter and are round, oval and sometimes triangular with
197 rounded corners. The skeletal chromites may be up to 5-6 cm across (Fig. 3B) and consist of
198 elongate blades of chromite with branches on each side. There are also triangular sections of
199 chromite with equi-dimensional sides (Fig. 3B1).

200

201 The orbicular chromitite consists of layers of chromite that appear to be draped around irregular
202 cores of dunite (Fig. 3 C and D). In one case a chromite triangle with cross bars of chromite occurs
203 with the skeletal chromites (Fig. 3E1) and in another a chromite nodule partially surrounds a
204 triangle structure with cross bars of chromite (Fig. 3F). The nodules containing skeletal chromites
205 enclose serpentinised olivine, clinopyroxene (now clinochlore) and plagioclase whereas the nodules
206 and skeletal crystals are surrounded only by serpentinised olivine. No sulfide or PGM phases such
207 as laurite or OsIrRu alloys were observed in these samples. Sulphur saturation and precipitation of
208 Pt- and Pd-bearing PGM did not occur in Cyprus until higher in the stratigraphy in the gabbro
209 (Prichard and Lord, 1990).

210

211 Figure 4 here

212

213 Cores from two samples from location 2 (Fig. 2) containing nodular chromite have been chosen for
214 3D imaging; ND 7 (Fig 4A) and ND 16 (Fig. 4B). The ND 7 core consists of nodular chromite
215 containing skeletal centres. Skeletal chromite occurs between these nodules (Fig. 4A). ND 16
216 consists of nodular chromite enclosing skeletal chromite but with less interstitial skeletal chromite.
217 The ND16 core is taken from a layer of nodular chromite. On the edge of this layer of nodules is

skeletal chromite with no rim of chromite surrounding it (Fig. 4B, #1). In the first row of chromite nodules along the edge of the nodular layer the skeletal chromite is totally (Fig. 4B#2) or partially (Fig. 4B#3) surrounded by a thin rim of chromite and further towards the centre of the layer of nodular chromite the skeletal chromite is completely surrounded by a thick rim of chromite (Fig. 4B#4). This progression of textures from the edge towards the centre of the nodule layer suggests that the skeletal crystals formed first and then the outer rim of chromite formed around them. ND 16 displays a variety of nodule shapes including those that are more angular than rounded. The outline of the skeletal chromite that forms the core of the nodule is reflected in the form of the outer nodule shell, and this gives rise to irregular shaped nodules; for example the rectangular nodule with rounded corners (located within the black square, Fig. 4B).

3.2 Nodules and skeletal crystals in 3D

High-resolution X-ray computed tomography (CT) provides 3D visualization of nodule structures and their core skeletal crystals. The CT data allow images to be examined in any chosen orientation, at 13 micron resolution throughout the volume of the sample analysed. Circular images (Fig. 5) across the core (Fig. 4A), chosen from 1043slices through this core, illustrate the textures of the skeletal and nodular chromite. The nodules and interstitial skeletal shapes of the chromite are clearly displayed and these are placed in context in the text that describes Fig. 9.

Figures 5 and 6 here

Silicates, including clinochlore, tremolite-actinolite and serpentine, are located between the skeletal chromite blades and are commonly completely enclosed by the nodule and isolated from the serpentine surrounding the nodule. It is also the case that silicates are trapped as inclusions between branches of skeletal chromite interstitial to the chromite nodules and are also isolated from the

244 surrounding silicate matrix, composed of serpentine after original olivine (Fig. 5).

245

246 The branches of chromite in skeletal crystals can be observed in 3D to extend to form a series of
247 parallel sheets (Fig. 6A). In 3D it is clear that the nodules usually touch one another and they may
248 also be interconnected with the interstitial skeletal chromite (Figs. 6B and D). Isolated octahedra of
249 chromite are also present between the chromite nodules (Fig. 6C).

250

251 *3.3 Electron Backscatter Diffraction (EBSD)*

252 A nodule containing skeletal chromite surrounded by a chromite rim, from the core that was
253 scanned using 3D X-ray tomography from sample ND 16, was selected for more detailed study.
254 Sections taken at right angles through the long axis of this nodule show a skeletal texture and a
255 double Y shape in the orthogonal section (Fig. 7A-C). The skeletal crystals are enclosed by a
256 chromite rim draping around the skeletal crystals and mimicking the shape of the outer surfaces of
257 the skeletal crystals (Figs. 4B and 7A-C).

258

259 Orientation mapping of the nodule reveals a core of skeletal crystals surrounded by grains up to
260 ~1mm in diameter that form a discrete rim around the core (Fig. 7D). The skeletal core displays a
261 much smaller range of orientations than the polycrystalline chromite grains in the rim (Fig. 7D).
262 Internally, the skeletal core records a limited range of orientations (Fig. 7D, F, G) but records lattice
263 distortions accommodated by discrete low-angle boundaries as well as a more subtle substructure
264 (Fig. 7D and E). In contrast, the rim grains tend to show smaller degrees of lattice distortion (Fig.
265 7D and E), although this is spatially quite heterogeneous (Fig. 7E, 8A-C), being preferentially
266 developed where the chromite grains impinge on a neighbouring nodule (Fig. 8C). The relationship
267 between the core and rim grains is also complex with most rim grains commonly showing
268 misorientation angles of 10-20° with adjacent parts of the core. However, a few grains show
269 misorientations as large as ~60°. These grains record a common {110} pole to the host (Fig. 7F and

G). The distribution of misorientation angles within the nodule indicates that the rim grains are not randomly-oriented with respect to the host, further indicating a crystallographic relationship between host and rim grains.

Figure 7 here

Figure 8 here

Chromite grains that make up the polycrystalline rim exhibit generally a smooth, but in detail crenulated, outer edge. Grain boundaries between the chromite grains in the rim are clearly truncated on the outer edge of the rim (e.g. Fig. 8A-D). Grain-scale microtextures within the rim range from random growth impingement with curved grain boundaries to well-developed adcumulate textures with equilibrium 120 degree grain boundaries (Fig. 7 D and E).

3.4. Chemical variability within the nodule

The chromite within the skeletal crystal and outer polycrystalline rim of the nodule analysed by point analyses (Fig. 8 D) and also mapped by energy dispersive spectrometry (EDS) in the course of the EBSD mapping shows that the chromite compositions across the entire nodule are remarkably similar throughout. SEM (EDS) element concentration maps for the selected sample are shown in Figs. 8 E and F. This indicates that the chromite aggregates are homogenous at a 50 micron scale within the precision of the analyses (plus or minus about 2% in FeO and Cr_2O_3) and that there is no detectable chemical zoning across the nodules.

The very edges of individual grains in the chromite rim are altered to a more Fe-rich and Mg- and Al-poor chromite. This alteration is common on the edges of all the grains in the rim of the nodule

(Fig. 8D, Table 1) and allows identification of the outlines of other grains in the rim as imaged by EBSD (Fig. 7 D and E). This feature also allows grain boundaries in granular rims to be identified in other nodules.

Table 1 here

The nodules are embedded in a matrix of olivine now altered to serpentine, the only other visible phase being Al-rich chlorite and a Ca-rich tremolite amphibole developed within the core of the prominent skeletal crystal-cored nodule (Fig. 8 E and F). This phase is interpreted as the product of alteration of the Ca and Al-bearing component of silicate melt trapped within the core framework.

4. Discussion

4.1 Formation of hopper crystals

The skeletal crystals show different stages of growth initially with just a few joined blades of chromite to more complete forms where blades are linked together enclosing silicates. In rapid crystallisation it is generally accepted that a crystallising component is added more quickly at crystal edges rather than in the centre of a crystal plane. In skeletal growth, fast growing facets extend through the depleted chemical boundary layer that forms around the growing skeletal crystal; in this way the fast-growth facets can continue to develop from undepleted solute, while other less favourable oriented facets have their growth inhibited by being starved of supply of their growth components. The resulting crystals are hopper shaped and are characterised by fully developed crystal edges with hollow interiors. Partially formed hopper crystals consist of complex intergrowths of formations (Fig. 9). A complete hopper crystal is also sometimes known as a skeletal cube (Phillips, 1965). Hopper crystals are commonly developed in crystals such as halite

322 and native bismuth. In 3D the Troodos skeletal crystals form hopper crystals and on 2D surfaces the
323 great variety of shapes correspond to sections across the hopper crystals.
324
325 Partially formed hopper crystals display complex growths that contain 3D arrow head structures
326 (Figs. 9 A and B). The fully formed hopper crystals consist of complete boxes where the arrow
327 heads have grown into cubes (Fig. 9 C). The 2D images of the skeletal crystals, both enclosed and
328 interstitial to chromite nodules, show a diversity of cross sections of hopper forms, with some of the
329 rarer forms including chromite triangles (Figs. 3B1, 5D2, 6D, 9J) with arrow shaped corners (Fig.
330 5B1), triangles containing partial (Fig. 5D1 also shown in 9F) or complete parallel blades linking
331 two sides of the triangle (Fig. 3E also shown in 9H) and a double Y shape (> −<) (Figs. 4C, 5C1,
332 7B and 9E and J). The 3D images of the skeletal crystals, both within and interstitial to the nodules,
333 show that they are actually formed of cages with hopper structures. It is also apparent that the
334 cage/hopper crystals are not always complete often having been in the process of growth as
335 crystallisation ceased (Figure 9D). Thus the arrow head textures and the triangles with partially
336 formed blades of chromite observed in 2D may be ascribed to partially formed cage/hopper crystals
337 (Figs. 9 E and F). The triangular chromite with skeletal parallel lines (Fig. 3F) is very similar to the
338 partially formed hopper crystal shown in Fig. 9B.
339
340 EBSD data show that the skeletal crystals recorded in the core of a nodule crystallise in a similar
341 orientation yet record a significant component of lattice distortion (Fig 7D-G). These variations in
342 orientation may be deformation-related features, related to late stages of solidification as noted for
343 zircon grains in andesite-derived cumulates (Reddy et al 2009). However, the lattice distortion is
344 greater than that recorded in rim grains and is therefore unlikely to represent only the effects of
345 post-rim deformation. More likely is that a component of the distortion represents the incorporation
346 of defects during growth of the hopper crystals. Such growth is widely recognised in non-geological
347 materials (e.g. Tiller 1991) and has been observed recently by EBSD in minerals crystallising from

348 melts and fluids (McLaren & Reddy 2008; Timms et al 2009).

349

350 The skeletal chromites studied here appear to be elongate cage/hopper crystals (Figs. 7A and 9).
351 The characteristic solid angle between the crystal faces shows that this skeletal core grew by
352 preferential development of <111> facets (Figs. 7F-G and 9G). This is consistent with the
353 orientation of dominant facets reported for dendritic chromite in komatiites by Godel et al. (2013).

354

355 Figure 9 here

356

357 As the skeletal crystals grow they joined up to form the cage/hopper structure illustrated in Fig 9G.
358 Cross sections such as observed in Fig. 3E (Fig. 9H), the almost complete double Y shape observed
359 in Fig. 5C (Fig. 9J), and the skeletal branching structure (Fig. 9K) can be explained as sections
360 across a complete or almost complete cage/hopper crystal.

361

362 4.2 *Origin of Troodos skeletal-cored chromite nodules*

363

364 Greenbaum (1977) concluded that the skeletal crystals in the centres of the chromite nodules from
365 Troodos, formed from supersaturation and /or supercooling of a magma and that there was a
366 continuous growth from skeletal crystals to massive nodules. Greenbaum (1977) did not comment
367 specifically on the conditions needed for the formation of the rim to the skeletal crystals. He
368 interpreted orbicular chromite as mechanical accretion of previously settled chromite grains around
369 a nucleus of dunite.

370

371 Leblanc (1980) re-examined these nodular and skeletal chromites from Troodos and agreed that
372 there was a sequence of textures from skeletal crystals with octahedral terminations and lamellae
373 (111) from initial Christmas tree forms becoming progressively in filled to form rounded nodules.

Euhedral terminations have the form (100), (110), (111) and (100). He concluded that the rounded surfaces are due to dissolution processes taking place in an open space moving environment.

4.3 Observations from the 3D study of these Troodos nodules

The results presented here broadly support the conclusions reached by Greenbaum (1977) and Leblanc (1980) using 2D observations. Interpretation of the 3D images corroborates the idea that these nodules formed by overgrowth of polycrystalline equant chromite aggregates onto pre-existing cores of skeletal chromite. The external shape of the nodule is determined by the shape of the accretion of the chromite rim draping over the skeletal crystal core. This gives the nodule either a spherical or a less regular more cubic shape but with rounded outer surfaces caused by the truncation of the granular rim. This demonstrates that the nodules grew from the centre outwards. There is no change in the composition of the chromite from the skeletal crystal outwards to the rim (Fig. 8 D, E and F) although it is possible that any such changes may have been lost due to later re-equilibration of the chromite.

A key observation in this study is that the grain orientations of the overgrown chromite rim are not random, but inherit a similar crystallographic orientation to that of the core skeletal crystal (Fig. 7 F, G). In cases where misorientation relationships between core and rim are large (~60°), the core and rim share a common {210} pole, further supporting a close crystallographic relationship between core and rim crystallography. This has an important implication: the rim accretion process is not mechanical, as this would produce random grain orientations, but rather is the consequence of heterogeneous nucleation of rim grains on the original skeletal crystal substrate. This has ramifications for current models of nodule formation, as discussed below.

The 3D images elucidate the growth history and explain the different chromite morphologies.

Initially skeletal chromite growth, driven by rapid crystallisation from Cr-supersaturated magma, forms elongate blades with <111> facets that nucleate side <111> branching out from the central blade (Fig. 10A). As growth proceeds the tips of the fastest growing branches extend through the depleted boundary layer around the rapidly growing skeletal crystal, and the tips spread sideways to form arrow shapes that in 3D appear as octahedral pyramids (Fig. 10B and Fig. 5C). In 3D the elongate skeletal growths often form a double Y shaped spine; as growth continues side plates from this double Y shaped spine grow and join, resulting in a cage structure rather than a branching structure. The growth of the side plates to join with the octahedral tips produces hopper structures on the faces of the cage (Fig.9).

As the degree of supersaturation in Cr decreases, skeletal growth ceases and further chromite growth takes place by heterogeneous nucleation of new grains on the skeletal chromite, followed by non-skeletal homogenous growth. A polycrystalline rim begins to form around the skeletal core, the growing equant crystals impinge to form curved non-faceted grain boundaries. Eventually a complete rim develops that encloses the skeletal crystal while mimicking its original external outline (Fig. 10C and C).

The EBSD data show that this nodule rim is made up of multiple crystals with rounded edges; these crystals grew adjacent to each other to form the coating around the skeletal grain. The undulatory outer surface of the nodule truncates grain boundaries of chromite grains in the rim, all the way around the entire nodule, and planar crystal facets are absent on the outer surface of the nodule. This suggests mechanical abrasion or partial dissolution of the nodule subsequent to crystallisation of the polycrystalline rim (Fig. 10D). This supports the idea of Leblanc (1980) that the smooth edge of the nodule is formed by dissolution and the observation that the nodules appear corroded (Thayer, 1964).

The EBSD data further show deformation of the chromite grains in the rim where nodules touch indicating that the nodules impinged on one another before the surrounding matrix to the nodules was completely solid, and after the truncation episode which we interpret as having happened while the nodules were still suspended in magma. The impingement could have occurred by transient collision as nodules settled, or during compaction and deformation of the nodule layer following accumulation of the nodule layer.

Figure 10 here

4.4 Evidence for quiescent conditions during nodule formation

The erosion of the outer surface of the nodule has been interpreted as the result of mechanical abrasion in a rapid flowing magma during formation as suggested by a number of authors (e.g Moghadam et al., 2009). Outcrops of nodular chromite may also display frozen flow structures interpreted as indicating rapid flow conditions (Huang et al., 2004). However this could equally well result from dissolution prior to consolidation. Barnes (1986) shows images of scalloped edges on chromite grains that had been heated experimentally above the liquidus of the enclosing melt and had undergone partial dissolution. The geometry is broadly similar to that of the nodule surfaces. The EBSD data (Fig. 8) indicate truncation of grains resulting in a smooth edge to the nodule but in detail this smooth surface is pitted or scalloped resulting from two stages of dissolution. It seems unlikely that the truncation is caused by erosion of the nodules in a rapidly flowing magma because the skeletal crystals external to the nodules are not broken and damaged. They would be so if the movement was sufficient to round and truncate the nodules. Indeed 3D imaging has shown that the skeletal crystals external to the nodules are commonly attached to the nodules. Partially formed hopper crystals could be preserved as they were forming or they may have been more complete and then subjected to dissolution.

This all mitigates against a change from quiescent to rapidly moving magma during the formation of skeletal crystals and then nodules, rather it supports the idea that the change from skeletal chromite formation to nodule formation is due to a change from supersaturation of the magma to one of crystallisation at equilibrium close to the liquidus, followed by dissolution in an environment of chromite undersaturation.

A previously suggested analogue for the formation of chromite nodules is the growth of sedimentary ooliths around irregular core fragments in as they roll in currents as is suggested for chromite nodules (Ahmed, 1982; Lago et al., 1982; Lorand and Ceuleneer, 1989; Thayer, 1969 and Dickey 1975). We are suggesting here that the skeletal crystals served as the original nuclei onto which the nodular chromite grew. A possibly more apposite analogy is the formation of graupel, which is soft hail or snow pellets formed from super cooled droplets freezing onto snowflakes, as described in Pinsky et al. (1998). Graupel grains attach to snowflakes producing a collection of grains that make up a rim around the skeletal snowflake. This is very similar to the texture observed in the Troodos nodules (Fig. 11).

Figure 11 here

4.5. Implications for in-situ adcumulus growth

An interesting feature of the granular chromite rim is that portions of it have evidently developed with equilibrium adcumulate textures with 120 degree triple point boundaries (Fig. 7 D). These textures are commonly interpreted in classical cumulus theory as forming due to annealing by filter pressing of trapped intercumulus liquid. However, this mechanism is clearly inapplicable here. An alternative mechanism involving in-situ growth of an adcumulate crust at the crystal liquid interface

478 has been proposed for the Jimberlana adcumulate, (Campbell, 1977; Campbell, 1987) and has been
479 demonstrated experimentally by Lesher and Walker (1988). The textures exhibited in the nodule rim
480 constitute observational evidence for this hypothesis. The alternative explanation is that the rims
481 have undergone recrystallisation and annealing, but this is inconsistent with the preservation of
482 highly disequilibrium skeletal crystal in the core. We interpret the adcumulus rim aggregates as the
483 result of highly efficient textural equilibration during near-liquidus growth of chromite in a well-
484 mixed, well stirred medium where boundary layers around the growing chromite grains were
485 disrupted by shear flow between the magma and the growing nodule, analogous to the in situ
486 growth of olivine adcumulates at the base of flowing komatiite lavas (Godel et al 2013).
487
488 *4.6. Implications for petrogenesis of nodular chromitite*
489
490 Matveev and Ballhaus (2002) have proposed an elegant and self-consistent model for the origin of
491 podiform chromitite based on physical collection of dispersed chromite grains by ascending vapour
492 bubbles within a water saturated boninite melt. Our observations in relation to their model are
493 somewhat equivocal. On one hand, sudden devolatilisation of a water-oversaturated magma
494 provides a mechanism for constitutional supercooling following a sudden pressure drop, and this
495 could provide an appealing mechanism for the initial formation of the skeletal crystal. On the other
496 hand, the spherically symmetrical deposition of skeletal and granular chromite in our nodule is hard
497 to reconcile with what would be an essentially stochastic process of mechanical entrainment of
498 chromite grains during bubble ascent; a random spatial disposition of grain shapes and sizes would
499 be expected within the nodule from what is purely a mechanical collection process. Our
500 observations are more consistent with sequential growth. Specifically, the preferential orientation of
501 the granular rim grain population towards the crystallographic orientation of the skeletal crystal
502 (Fig.7) argues strongly for a heterogeneous nucleation control rather than purely chance physical
503 agglomeration. The presence of localised patches of adcumulate texture within the rim has the same

implication. Furthermore, our observations attest to a post-growth dissolution mechanism to produce the rounded outer surface of the nodule, which in the Matveev and Ballhaus model is attributed to the surface tension-controlled outer surface of the entraining moving bubble. Our observations suggest a general lack of movement during nodular rim formation. In summary, while our observations do not disprove the bubble-collection hypothesis, they strongly favour a mechanism of accretionary growth.

5. Conclusions

A combination of microcharacterisation techniques on spectacular samples of skeletal-cored chromite nodules provides new insights into crystallisation mechanisms. The key observations are:

1) the skeletal core is a single crystal, formed by rapid preferential growth of <111>facets, as observed in skeletal chromites from other settings;

2) the core is surrounded by a polycrystalline rim showing non-random crystallographic relationships to the host skeletal crystal core implying that the rim formed by accretionary crystal growth, and not by mechanical agglomeration;

3) the nodule rim contains domains of adcumulate texture implying that such textures can form as primary crystallisation features and do not require mechanisms such as trapped liquid expulsion; further, adcumulate textures in chromitites do not require recrystallization, but can be the direct result of primary crystallisation from the magma at its liquidus;

4) grain boundaries in this rim are truncated by an undulose outer surface on the nodule that was predominantly formed by dissolution of the nodule after incorporation into chromite undersaturated magma;

5) minor deformation of the nodule occurred at a late stage, preferentially at impingement points with neighbours.

530 The evidence presented here implies that skeletal chromite cores to nodules from the Troodos
531 ophiolite formed first and were then coated with individual chromite grains, indicating that the
532 nodules grew from the centre outwards. As observed in 3D the skeletal crystals are likely to have
533 grown rapidly along preferred fast-growing crystallographic directions in a regime of chromite
534 supersaturation, forming blades of chromite that produce a cage/hopper structure elongated along
535 <111>. Then, as the degree of supersaturation decreased, the rate of chromite nucleation increased
536 relative to the rate of growth, and multiple individual grains formed around the skeletal crystals.
537 These aggregated to produce a rim that retains the overall geometric outline of the skeletal crystal.
538 This accounts for the crystal-like morphology of the entire polycrystalline nodule. Truncation of the
539 grains on the edge of the rim suggests that the nodules were subsequently partially dissolved, in a
540 chromite undersaturated magma. Then at some point post formation the nodules collided and were
541 deformed at impingement points.
542
543 The disposition of crystal shapes and orientations in the nodule is considered to be inconsistent with
544 a process of mechanical collection of pre-existing chromite grains by vapour bubbles. The observed
545 textures record sequential crystallisation of a suspended crystal aggregate under varying degrees of
546 chromite saturation. The progression from skeletal crystals in the core to equant polycrystalline rim
547 to subsequent resorption records a growth sequence influenced by changing chemical
548 environments: initial growth from chromite-supersaturated magma allowed skeletal crystal growth,
549 followed by breakdown of chemical boundary layers giving rise to granular growth in preferred
550 orientations and in local textural equilibrium. Subsequent incorporation of the nodule into chromite
551 undersaturated magma gave rise to dissolution and truncation of pre-existing grain boundaries at the
552 edge of the nodule rim.
553
554 Nodular chromite without skeletal cores is commonly described from ophiolite complexes. The
555 growth of these Cypriot nodules by accumulation of granular chromite to form polygranular rims

around a skeletal nucleus may be a more widespread process in the formation of the more common types of nodular chromite which do not preserve visual evidence of skeletal crystals in their cores but may have formed in a similar way by growth around a nucleus. The observations described here, made possible by the use of 3D tomography and EBSD, may also point to a key link in the understanding of the process of podiform chromitite formation in ophiolites in general. The formation of the chromite nodules suggests that the magma fluctuates from Cr oversaturated to under saturated and may indicate that chromitite in ophiolite complexes forms in a regime that oscillates from supersaturated, supercooled conditions to conditions of chromite undersaturation Our observations attest to the formation of chromite nodules in a magmatic environment of fluctuating cooling rate and magma composition.

Acknowledgements

Hazel Prichard would like to thank the CSIRO Office of the Chief Executive (OCE) for funding this research during a Distinguished Visiting Fellowship. Angela Halfpenny is funded by the CSIRO OCE Postdoctoral Fellowship scheme. Zoja Vukmanovic and Steve Reddy acknowledge support through the Australian Research Council Core to Crust Fluid Systems Centre of Excellence and ARC LIEF Funding. Mark Pearce is thanked for contributing to the interpretation of the EBSD images, and along with Patrick Nadoll for a very thorough review of an early draft. This is an output of the CSIRO Minerals Down Under National Research Flagship.

References

Ahmed, Z., 1982. Porphyritic-nodular, nodular, and orbicular chrome ores from the Sakhakot-Qila complex, Pakistan, and their chemical variations. Mineralogical Magazine 45, 167-178.

582 Ahmed, A.H., Arai, S., Attia, A.K., 2001. Petrological characteristics of podiform chromitites and
583 associated peridotites of the Pan African Proterozoic ophiolite complexes Egypt. Mineralium
584 Deposita 36, 72-84.
585
586 Arai, S., Yurimoto, H., 1994. Podiform chromitites of the Tari-Misaka ultramafic complex,
587 southwestern Japan, as mantle-melt interaction products. Economic Geology 89, 1279-1288.
588
589 Ballhaus, C., 1998. Origin of podiform chromite deposits by magma mingling. Earth and Planetary
590 Science Letters 156, 185-193.
591
592 Barnes, S.J., 1986. The distribution of chromium among orthopyroxene, spinel and silicate liquid at
593 atmospheric pressure: Geochimica et Cosmochimica Acta. 50, 1889-1909.
594
595 Brown, M., 1980. Textural and geochemical evidence for the origin of' some chromite deposits in
596 the Oman ophiolite, in: Panayiotou, A., (Ed.), Ophiolites. Proceedings of the International Ophiolite
597 Symposium, Cyprus, pp. 714-721.
598
599 Campbell, I.H., 1977. A study of macrorhythmic layering and cumulate processes in the Jimberlana
600 Intrusion, Western Australia, Part I: The upper layered series. J. Petrol. 18, 183-215.
601
602 Campbell, I.H., 1987. Distribution of orthocumulate textures in the Jimberlana Intrusion. J. Geol.
603 95, 35-54.
604
605 Ceuleneer, G., Nicolas, A., 1985. Structures in podiform chromite from the Maqsad District (Sumail
606 Ophiolite, Oman). Mineralium Deposita 20, 177-185.
607

608 Christiansen, F.G., Olesen, N.O., 1990. Large skeletal chromites in the Vourinos ophiolite, Greece.
609 Bulletin of the Geological Society of Denmark 38, 33-42.
610
611 Dickey, J.S.Jr., 1975. A hypothesis of origin for podiform chromite deposits. Geochimica
612 Cosmochimica Acta, 39, 1061-1074.
613
614 Dilek, Y., 2003. Ophiolite concept and its evolution, in: Dilek, Y., Newcomb, S., (Eds.), Ophiolite
615 Concept and the Evolution of Geological Thought, Geological Society of America Special Paper
616 373, pp. 1–16.
617
618 Dowling, S.E., Barnes, S.J., Hill, R.E.T., Hicks, J., 2004. Komatiites and Nickel Sulphide Ores of
619 the Black Swan area, Yilgarn Craton, Western Australia. 2. Geology and Genesis of the Orebodies.
620 Mineralium Deposita 39, 707-728.
621
622 Economou-Eliopoulos, M., 1996. PGE distribution in chromite ores from ophiolite complexes:
623 implications for their exploration. Ore Geology Reviews 11, 363-381.
624
625 Godel, B., 2013. High-resolution X-ray computed tomography and its application to ore deposits:
626 from data acquisition to quantitative three-dimensional measurements with case studies from Ni-
627 Cu-PGE deposits; Economic Geology 108, 2005-2019.
628
629 Godel, B., Barnes, S.J., Gurer, D., Austin, P. Fiorentini, M.L., 2013. Chromite in komatiites: 3D
630 morphologies with implications for crystallization mechanisms. Contributions to Mineralogy and
631 Petrology 165, 173-189.
632
633 Golding, H.G., 1975. Relict textures of chromitites from New South Wales. Journal of the

634 Geologial Society of Australia 22, 397-412.
635
636 González-Jiménez, J. M., Griffin, W. L., Proenza, A., Gervilla, F., O'Reilly S. Y., Akbulut, M.,
637 Pearson, N. J., Arai, S., 2014. Chromitites in ophiolites: How, where,when, why? Part II. The
638 crystallisation of chromitites. Lithos 190-191, 520- in press.
639
640 Greenbaum, D., 1977. The Chromitiferous rocks of the Troodos ophiolite, Cyprus. Economic
641 Geology 72, 1175-1194.
642
643 Groves, D.I., Barrett, F.M., Binns, R.A., McQueen, K.G., 1977. Spinel phases associated with
644 metamorphosed volcanic-type iron–nickel sulphide ores from Western Australia. Economic
645 Geology 72, 1224–1244.
646
647 Halfpenny, A., 2010. Some important practical issues for collection and manipulation of electron
648 backscatter diffraction (EBSD) data from rocks and minerals. Journal of the Virtual Explorer 35, 1-
649 18.
650
651 Halfpenny, A., Hough, R.M., Verrall, M., 2013. Preparation of samples with both hard and soft
652 phases for electron backscatter diffraction: Examples from gold mineralisation. Microscopy and
653 Microanalysis 19, 1007-1018.
654
655 Huang, X., Li, J., Kusky, T.M., Chen, Z., 2004. Microstructures of the Zunhua 2.50 Ga podiform
656 chromite, North China Craton and implications for the deformation and rheology of the Archaean
657 oceanic lithospheric mantle, in: Kusky, T.M., (Ed.) Precambrian ophiolites and related rocks,
658 Developments in Precambrian geology Chapter 10, 13 (K C Condie series Ed.) pp. 321-337.
659

660 Irvine, T.N., 1977. Origin of chromitite layers in the Muskox intrusion and other stratiform
661 intrusions: A new interpretation. Geology 5, 273–7.
662
663 Jackson, E.D., 1969. Chemical variation in coexisting chromite and olivine in chromitite zone of the
664 Stillwater Complex, in Wilson H.D.B. (Ed.), Magmatic Ore Deposit Economic Geology
665 Monograph 4, 41– 71.
666
667 Keleman, P.B., 1995. Extraction of mid-ocean ridge basalt from the upwelling mantle by focused
668 flow of melt in dunite channels. Nature 375, 747-753.
669
670 Lago, B.L., Rabinowicz, M., Nicolas, A., 1982. Podiform chromite orebodies: a genetic model.
671 Journal Petrology 23, 103-125.
672
673 Leblanc, M., 1980. Chromite growth, dissolution and deformation from a morphological view
674 point: SEM investigations. Mineralium Deposita 15, 201-210.
675
676 Leblanc, M., Ceuleneer, G., 1992. Chromite crystallization in a multicellular magma flow:Evidence
677 from a chromitite dike in the Oman ophiolite. Lithos 27, 231-257.
678
679 Lesher, C.E., Walker, D., 1988. Cumulate maturation and melt migration in a temperature gradient.
680 J. Geophys. Res. 93B, 10295-10311.
681
682 Lorand, J.P., Ceuleneer, G., 1989. Silicate and base-metal sulphide inclusions in chromites from the
683 Maqsad area (Oman ophiolite, Gulf of Oman): A model for entrapment. Lithos 22, 173-190.
684
685 Naldrett, A.J., Kinnaird, J.A., Wilson, A., Yudovskaya, M.A., McQuade, S., Chunnett, G., Stanley,

C., 2009. Chromite composition and PGE content of Bushveld chromitites: Part 1 - the Lower and Middle Groups. Transactions of the Institute Mining and Metallurgy B 118, 131-161.

Matveev, S., Ballhaus, C., 2002. Role of water in the origin of podiform chromitite deposits: Earth and Planetary Science Letters 203, 235–243.

Sandra McLaren, S., Reddy, S. M., 2008. Automated mapping of K-feldspar by electron backscatter diffraction and application to 40Ar/39Ar dating:Journal of Structural Geology 30, 1229–1241.

Melcher, F., Grum, W., Simon, G., Thalhammer, V.T., Stumpfl E.F., 1997. Petrogenesis of the ophiolitic giant chromite deposits of Kempirsai, Kazakhstan: a study of solid and fluid inclusions in chromite. Journal of Petrology 38, 1419–1458.

Moghadam, H.S., Rahgoshay, M., Forouzesh, V., 2009. Geocheomical investigation of nodular chromites in the Forumad ophiolite, NE of Iran. Iranian Journal of Science and Technology, Transactions A 33,103-108.

Morishita, T., Andal, E.S., Arai, S., Shida, V.I., 2006. Podiform chromitites in the lherzolite-dominant mantle section of the Isabela ophiolite, the Philippines. Island Arc 15**,** 84–101.

Pagé, P., Barnes, S-J., 2009. Using trace elements in chromites to constrain the origin of podiform chromitites in the Thetford Mines ophiolite, Québec, Canada. Economic Geology 104, 997–1018.

Paktunc, A.D., 1990. Origin of podiform chromite deposits by multistage melting, melt segregation and magma mixing in the upper mantle. Ore Geology Reviews 5, 211-222.

712 Pavlov, N.V., Grigoryeva, I., Tsepin, A.I., 1977. Chromite nodules as an indicator of liquation of a
713 magmatic melt: International Geology Reviews 19, 43-56.
714
715 Phillips, F. C., 1971. An introduction to crystallography, fourth ed.. Oliver and Boyd, Edinburgh.
716
717 Pinsky, M., Khain, A., Rosenfeld, D., Pokrovsky, A., 1998. Comparison of collision velocity
718 differences of drops and graupel particles in a very turbulent cloud: Atmospheric Research 49, 99-
719 113.
720
721 Prior, D.J., Boyle, A. P., Brenker, F., Cheadle, M. C., Day, A., et al., 1999. The application of
722 electron backscatter diffraction and orientation contrast imaging in the SEM to textural problems in
723 rocks. American Mineralogist 84, 11-12,1741-1759.
724
725 Prior, D.J., Mariani, E., Wheeler, J., 2009. EBSD in the earth sciences: applications, common
726 practice and challenges, in Schwartz, A.J., Kumar, M., Adams, B.L., Field, D.P., (Ed.), Electron
727 Backscatter Diffraction in Materials Science, Berlin, Springer, 345-360.
728
729 Prichard, H.M., Neary, C.R., 1982. Some observations on the chromite in the Shetland
730 ophiolite complex. Ofioliti 2/3, 455-466.
731
732 Prichard, H.M., Lord, R.A., 1990. Platinum and palladium in the Troodos ophiolite complex,
733 Cyprus. Canadian Mineralogist 28, 607-617.
734
735 Prichard, H.M., Brough, C., 2009. Potential of ophiolite complexes to host PGE deposits. In New
736 developments in magmatic Ni-Cu and PGE deposits, in: Li, C., Ripley E.M. (Eds.) Geological
737 publishing house Beijing, pp. 277-290.

738

739 Proenza, J., Gervilla, F., Melgarejo, J.C., Bodinier. J. L., 1999. A1-and Cr-Rich chromitites from the
740 Mayari-Baracoa ophiolitic Belt (Eastern Cuba): Consequence of Interaction between volatile-rich
741 melts and peridotites in suprasubduction mantle. Economic Geology 94, 547-566.

742

743 Roberts, S., Neary, C.R., 1993. Petrogenesis of ophiolitic chromitite, in Prichard, H.M., Alabaster,
744 T., Harris, N.B.W., Neary, C.R., (Eds.), Magmatic processes and plate tectonics: Geological Society
745 of London, Special Publication 76, 257–272.

746

747 Rynearson, G.A., Smith, C.T., 1940. Chromite deposits in the Seiad Quadrangle Siskiyou county,
748 California: strategic minerals investigations. Bulletin 922-J, 281-306.

749

750 Tarkian, M., Naidenova, E., Zhelyaskova-Panayotova, M., 1991. PGM in chromitites from the
751 eastern Rhodope ultramafic complex, Bulgaria. Mineralogy and Petrology 44, 73-87.

752

753 Thayer, T.P., 1964. Principal features and origin podiform chromite deposits, and some observations
754 on the Guleman-Soridag district, Turkey. Economic Geology 59, 1497-1524.

755

756 Thayer, T.P., 1969. Gravity differentiation and magmatic re-emplacement of podiform chromite
757 Deposits, in: Wilson, H.D.B. (ed.) Magmatic Ore Deposits, Economic Geology Monograph 4, pp
758 132-146.

759

760 Tiller, W. A. 1991. The Science pf crystallisation: macroscopic phenomena and defect generation.
761 Cambridge University Press, UK.

762

763 Timms, N. E., Li, J., Reddy, S. M. 2009. Quantitative microstructural characterization of
764 natrojarosite scale formed during high-pressure acid leaching of lateritic nickel ore: American
765 Mineralogist 94, 1111–1119.
766
767 Uysal, I., Sadiklar, M. B., Tarkian, M., Karsli, O., Aydin, F., 2005. Mineralogy and composition
768 of the chromitites and their platinum-group minerals from Ortaca (Mugˇla-SW Turkey): evidence
769 for ophiolitic chromitite genesis. Mineralogy and Petrology 8, 219–242.
770
771 Van der Kaaden, G., 1970. Chromite-bearing ultramafic and related gabbroic rocks and their
772 relationship to "ophiolitic" extrusive basic rocks and diabases in Turkey. Geological Society of
773 South Africa Special Publication 1, 511-531.
774
775 Xu, X., Yang, J., Ba, D., Guo, G., Robinson, P.T., Li, J., 2011. Petrogenesis of the Kangjinla
776 peridotite in the Luobusa ophiolite, southern Tibet. Journal of Asian Earth Sciences 42, 553-568.
777
778 Zhou, M.-F., Malpas, J., Robinson, P.T., Sun, M., Li, J.-W., 2001. Crystallisation of podiform
779 chromites from silicate magmas and the formation of nodular textures. Resource Geology 5, 1-6.
780
781 Zhou, M.-F., Robinson, P. T., Malpas, J., Li, Z., 1996. Podiform chromitites in the Luobusa
782 ophiolite (SouthernTibet): Implications for Melt-Rock Interaction and Chromite Segregation in the Upper
783 Mantle. Journal of Petrology 37, 3-21.

Figure captions

Fig. 1 Map of the global distribution of Proterozoic and Phanerozoic ophiolite belts modified from Dilek (2003) showing the distribution of ophiolites with podiform chromitite from (Prichard and Brough, 2009) including those that contain nodular chromite of all ages including (1) taken from Rynearson and Smith (1940), Arai and Yurimoto (1994), Morishita et al. (2006), (2) Economou-Eliopoulos (1996), Tarkian et al. (1991), Paktunc (1990), Brown (1980), Ahmed (1982), Zhou et al. (1996), Proenza et al. (1999), (3) Pagé and Barnes (2009), Prichard and Neary (1982), Melcher et al. (1997), (4) Golding (1975), (5) Ahmed et al. (2001), Huang et al. (2004).

Fig. 2 Chromite occurrences on Mt Olympus including the sample localities for the samples studied here (2 and 3), (adapted from Greenbaum, 1977).

Fig. 3 Photographs of samples collected from localities 2 and 3 in Troodos (Fig. 1). **A**, Layer of nodules with skeletal crystals between nodules, on the edge of the nodule layer and into the adjacent dunite, **B**, Patch of skeletal chromite including a triangular cross section (1), **C** and **D**, examples of orbicular chromite showing chromite rims around irregular clasts of dunite, **E**, Skeletal chromite in dunite close to a layer of nodules. Skeletal crystals include a chromite triangle with cross branches of chromite that with 3D imaging are seen to be part of a well-developed cage structure (1), **F**, Triangular shaped skeletal chromite with internal cross branches of chromite partially surrounded by nodular chromite with smooth outer surfaces.

Fig. 4 A, Sample ND 7 Skeletal crystals located between and on the edge of a group of

chromite nodules. **B,** Sample ND 16 A group of chromite nodules (black) in serpentine with skeletal crystals showing stages of chromite rim development, from the edge to the centre of the group of nodules (1) no rim, (2) a thin rim, (3) a partial rim and (4) a thick rim. The nodule chosen for EBSD analysis is located within the black square.

Fig. 5 Circular slices of ND7 core outlined by a black circle. Chromite (black) serpentine (grey) and enclosed silicates (white). Core is circular with a diameter of 25mm; note the slice is viewed at a slight angle and so does not quite appear circular. **A** is a typical section of core (slice 561). Specific features include **B** a triangle of chromite with lateral spurs parallel to the spur of the arrow head shaped corner of the triangle (1) (slice 592). **C** double Y-shaped structure with cross bars (1) (slice 642) and **D** an elongate triangle with a skeletal crystal attached to one side (1) and an equilateral triangle of chromite (2) (slice 708).

Fig. 6 A, 3D image of a cage structure of chromite showing truncation of the cage that reveals the 2D skeletal form (black). Blades that make up this 2D skeletal crystal extend in 3D to form parallel plates that make up part of a cage structure. **B-D**, are 3D images from ND16. Outer surfaces are shown in light grey and internal surfaces within nodules are shown in darker shades. **B-D** are all shown at the same scale. **B,** Nodules touching each other, **C**, Euhedral octahedral shaped chromite located in between chromite nodules and **D**, nodules interconnected with skeletal chromite. Note the smooth outer surfaces of the nodules, also evident in B.

Fig. 7 Images of the nodule ND16 chosen for EBSD analysis. The nodule is identified by a white square in **A** and also by a square in Fig. 4B. **A,** Three slices selected from the CT slices taken at right angles across the nodule; two across the elongate axis of the nodule (rectangles)

and a third section at right-angles to these sections (square). **B,** 3D image of the chromite nodule with the edge outlined (black dashed line). The 3D image shows the chromite rim and the central skeletal crystal structure forming a double Y shape. **C,** Atomic number contrast image of the nodular chromite containing a core skeletal crystal black box outlines the EBSD image in Fig. 8. **D** Large area orientation map of the chromite nodule created from combined stage and beam scanning of the sample to yield a 689 x 591 pixel map with step size of 13.57 μm. Colours represent the misorientation angle (up to 64°) from the orientation at the point marked by the white cross. Grain boundaries (>10°) and low angle boundaries (2-10°) are shown in black and red respectively. **E** Disorientation map, created from same data as **D**, showing misorientation axis and angle relationships within single grains of the nodule. The average orientation (grey center of the circular scale) of each grain is compared to each orientation within the grain and a color assigned based on the axis orientation and misorientation angle. The resulting figure shows the amount of lattice distortion within individual grains that make up the nodule. **F** Pole figures of chromite {100}, {110} and {111} poles. Colors correspond to those shown in **D**. **G** Inverse pole figures showing the distribution of sample coordinates (X,Y,Z) shown in **D** within the crystal coordinate framework. Colors correspond to those shown in **D**.

Fig. 8

A-D, Close up of part of the nodule as shown in the box in Fig. 8F. **A,** Orientation map of the chromites displayed as a sum of three Euler angles. An area at the bottom shows a portion of the skeletal crystal at the bottom in uniform pale green implying the same orientation of the crystal domains. This is separated by a black line from the rim of the nodule which hosts areas of different colours implying that these grains are differently orientated and two of these grains are imaged in **B** and **C**. **B-C** These show band contrast - local misorientation map of two domains including analyses 6 – 8 **E** and 9 – 11 **F**. Colors indicate the angle of

misorientation between each point on the grain and an arbitrary reference point located in the dark blue area within the grain. **B** Small variations (up to 4°) are displayed as misorientations in a chromite grain in the rim. The grain is cross-cut by brittle fractures. **C** Greater changes in internal orientation (up to 10°) shown in this chromite grain in the rim located at a point where it is in contact with a neighbouring chromite nodule. This is in contrast to the adjacent grain **B** where the orientation range is much more restricted. **D** Backscattered electron image showing locations of chromite analyses, 1-3 skeletal crystal, 4-11 chromite rim grains and 12-13 altered rims of grains (Table 1). The lighter grey material is Fe-enriched alteration at each chromite grain boundary as seen on the EBSD image in **A**. The silicates are shown in dark grey; black represents cracks and the space around the nodule. **E, F,** SEM (EDS) RGB elemental maps of the chromite nodule, where in **E** red represents Al, green represents Ca and blue represents Al and in **F** red represents Al, green represents Mg and blue represents Fe. Images show a high degree of homogeneity within and between the skeletal-cored chromite nodules. Note Al-rich phase(s) in cores of three of the larger nodules are absent outside the nodules. The dominant interstitial phase is serpentinised olivine.

Fig. 9 Sketches of growth stages of a skeletal crystal in 3D, growth of the structure to form the cage/hopper structure. Grey images are parts of slices taken across the skeletal crystals analysed using high-resolution X-ray computed tomography and one image **H** is from a polished section. **A** and **B** are sketches of native bismuth adapted from http://www.cuttingrocks.com/gallery_culturedcrystals1.shtml **D-K** are of the skeletal chromite that are the focus of this study. **C** is a fully formed cage/hopper crystal. **D** is a sketch of the skeletal chromite in process of growth into a cage/hopper crystal. **E** is a sketch of a 2D section across the partially formed cage/hopper crystal accompanied by an imaged slice from ND 7 (shown in Fig. 5C1). **F** is an imaged slice taken parallel to the long axis of the partially

formed cage/hopper crystal of chromite (also shown in Fig. 5D1). **G** is a skeletal crystal that is complete and forms an elongate hopper crystal. **H** (shown in Fig. 3E), **J** (from ND-7 slice 690) and **K** are slices through a complete hopper crystal.

Fig. 10 Model showing the stages of growth of the nodules with skeletal cores from Troodos revealed by analysis of the 3D images and the EBSD, **A**, Initial rapid skeletal crystal growth, **B**, Heterogeneous nucleation of granular chromite around edges of the partially formed skeletal core, **C**, Ongoing growth of granular chromite, textural maturation producing adcumulate domains, **D**, Dissolution of the chromite rim producing a smooth rounded margin and truncated rim grains. Approximate diameter of the nodule is 1 cm.

Fig. 11 SEM image of frozen water droplets or graupel (up to 50 μm in diameter) on the surface of a snow crystal formed by accretion. Crystals that exhibit frozen droplets on their surfaces are known as rimed. (http://emu.arsusda.gov/snowsite/rimegraupel/rg.html). Electron and Confocal Microscopy Laboratory, Agricultural Research Service, U. S. Department of Agriculture.

The structure and origin of nodular chromite from the Troodos ophiolite, Cyprus, revealed using high-resolution X-ray computed tomography and Electron Backscatter Diffraction

H. M. Prichard[a], S. J. Barnes[b] , B. Godel [b], S. M. Reddy[c] , Z. Vukmanovic[c], A. Halfpenny[d] , C. R. Neary[a] and P. C. Fisher[a]

a School of Earth and Ocean Sciences, Cardiff University, Cardiff, CF10 3AT, Wales, UK.
b CSIRO Earth Science and Resource Engineering, ARRC, 26 Dick Perry Avenue, Kensington, WA, 6151, Australia.
c Dept. Of Applied Geology, Curtin University, Kent St., Bentley, WA 6102, Australia
d Electron Microscopy Facility, Department of Imaging and Applied Physics, Curtain University, GPO Box U1987, Perth, WA 6845, Australia.

Prichard@cardiff.ac.uk corresponding author 0044 2920484731

Key words Chromite, nodule, skeletal crystal, hopper crystal.

Abstract

Nodular chromite is a characteristic feature of ophiolitic podiform chromitite and there has been much debate about how it forms. Nodular chromite from the Troodos ophiolite in Cyprus is unusual in that it contains skeletal crystals enclosed within the centres of the nodules and interstitial to them. 3D imaging and electron backscatter diffraction have shown that the skeletal crystals within the nodules are single crystals that are surrounded by a rim of polycrystalline chromite. 3D analysis reveals that the skeletal crystals are partially or completely formed cage or hopper structures elongated along the <111> axis. The rim is composed of a patchwork of chromite grains that are truncated on the outer edge of the rim. The skeletal crystals formed first from a magma supersaturated in chromite and silicate minerals crystallised from melt trapped between the chromite skeletal crystal blades as they grew. The formation of skeletal crystals was followed by a crystallisation event which formed a silicate-poor rim of chromite grains around the skeletal crystals. These crystals show a weak preferred orientation related to the orientation of the core skeletal crystal implying that they formed by nucleation and growth on this core, and did not form

by random mechanical aggregation. Patches of equilibrium adcumulate textures within the rim attest to in situ development of such textures. The nodules were subsequently exposed to chromite undersaturated magma resulting in dissolution, recorded by truncated grain boundaries in the rim and a smooth outer surface to the nodule. None of these stages of formation require a turbulent magma. Lastly the nodules impinged on each other causing local deformation at points of contact.

1. Introduction

Fossilised oceanic crust or ophiolite complexes often contain podiform chromitite. These are bodies of massive high chromium chromite that are commonly economically viable orebodies, as in Kazakhstan (e.g. Melcher et al., 1997). Podiform chromitites are located within mantle harzburgite surrounded by a lens of dunite and are often found in the transition zone between the mantle and overlying crustal dunite, as well as in the dunite itself (Pagé et al., 2009; Roberts and Neary, 1993; Prichard and Neary, 1982; Thayer, 1964; Uysal, 2005; González-Jiménez et al., 2014). Much of a typical podiform chromitite is composed of massive granular chromite, but the pods are also often made up of stacks of discontinuous layers of chromitite. Nodular and orbicular chromite are common components of podiform chromitite in many ophiolites of all ages and have been described by many authors (Fig. 1), e.g. from California (Ryerson and Smith 1940), Cuba (Thayer, 1964), Oman (Brown, 1980), Pakistan (Ahmed, 1982), Turkey (Paktunc, 1989), northern China (Huang et al., 2004) and southern Tibet (Xu et al., 2011).

The origin of nodular chromite is controversial as is the origin of podiform chromitite. Nodular and orbicular chromite, although not the major forms of chromite in podiform chromitite, provide important clues to the mode of formation of this style of deposit. In this contribution, we provide new microtextural information on a rare variety of nodular chromite associated with skeletal chromite that provides a unique insight into the contentious question of how chromite nodules crystallise.

Figure 1 here.

Nodular chromite is restricted to ophiolitic chromitite and is absent from stratiform chromitite in layered intrusions (Matveev and Ballhaus, 2002), such as the Bushveld complex in South Africa, (e.g Irvine, 1977; Jackson, 1968; Naldrett, 2009). The restriction of the occurrence of nodular chromite to ophiolite complexes indicates a formation mechanism that is unique to an oceanic setting.

Nodules of chromite range from 2-30 mm in size and are approximately spherical or ovoid in shape. They can however have flat surfaces giving the nodules distinctive cubic shapes with rounded corners (Ceuleneer and Nicholas, 1985). The nodules usually have fairly smooth outer surfaces and are mostly composed of chromite. They are commonly associated with euhedral chromite grains, as first described by Thayer (1969). Nodules generally occur in groups, often in layers and may be in contact with each other (Ahmed, 1982) sometimes appearing to have collided with each other causing deformation of the nodules (e.g. Paktunc, 1990; Prichard and Neary, 1982). Nodular ore types are typically restricted to the peripheries of the ore bodies or to smallish ore bodies, usually they occur in close proximity to the dunite halo (Ballhaus pers. comme).

Chromite in some cases forms rims around cores of silicates producing orbicular chromite or chromite anti-nodules (Brown, 1980). Multiple thin shells of alternating chromite and olivine form more complex orbicular chromite (Ahmed, 1982; Dickey, 1975; Greenbaum, 1977; Huang et al., 2004; Melcher, 1977; Thayer, 1969; Zhou et al., 2001).

There is no agreement on how these nodules form or even whether the nodules crystallised inwards towards the core or grew from the centre outwards. Nodules have been reported to lack chemical

zoning (Ahmed, 1982; Greenbaum, 1977). Other researchers report chemical differences towards the rim including Cr decrease and Ti increase (Leblanc and Ceuleneer, 1992).

In rare cases the nodules can have skeletal chromite in their cores. Examples include the samples from the Troodos ophiolite complex presented in this study and by Greenbaum (1977). Skeletal chromite has also been reported from the Vourinos ophiolite complex in Greece (Christiansen and Olesen, 1990) and the Zunhua ophiolite in northern China (Huang et al., 2004). Skeletal chromite has also been described from komatiites (e.g. Godel et al., 2013) from spinifex-textured flow tops and coarse grained olivine cumulates and also within massive sulphide ores at the contact with overlying komatiite flows (Dowling et al., 2004; Groves et al., 1977). However, these skeletal grains lack the distinctive association with nodules reported here. Skeletal chromite has been interpreted as the result of rapid crystal growth from chromite-supersaturated magma (Godel et al., 2013). This is also the process suggested by Greenbaum (1977) for the formation of the nodules associated with skeletal forms from Cyprus.

1.1 Hypotheses for the origin of nodular and orbicular chromite

There have been many mechanisms suggested for the growth of nodular and orbicular chromite. The main theories include:

(1) Growth from suspended aggregates of chromite accumulating concentrically in fast flowing magma (Huang et al., 2004) with aggregation, and coalescence or clustering of free-formed chromite grains prior to settling (Ahmed, 1982; Lago et al., 1982; Lorand and Ceuleneer, 1989; Thayer, 1969) and similarly snowballing in a turbulent flow as suggested by Dickey (1975).

(2) Separation from already consolidated chromite ore and abrasion during rock flowage (van der Kaaden, 1970).

(3) Collection of chromite from silicate magma during magma mingling by its attachment to a water-rich fluid that forms an envelope around the chromite producing spherical aggregates (Ballhaus, 1998; Matveev and Ballhaus, 2002).

(4) Formation in turbulent picritic magma flow accompanied by a water-rich fluid (Moghadam et al., 2009).

(5) Solidification of globules from a (hypothetical) chromite-rich immiscible liquid (Pavlov, 1977).

(6) Association with silica-rich droplets arising from wall-rock reaction causing chromite crystallisation around the droplet and their 'collapse' to form chromite nodules (Zhou et al., 2001). This builds on the ideas of magma processes in oceanic mantle developed by Keleman (1995).

Figure 2 here

1.2 Sample locations

This paper presents results of a study of a suite of samples from the Troodos Ophiolite. The Troodos Mountains in Cyprus host the classic ophiolite sequence exposed on Mt Olympus : mantle harzburgite is surrounded and overlain by dunite, wehrlite and pyroxenite that are in turn overlain by gabbro. The whole sequence is truncated and dissected into blocks by faulting. Podiform chromitite is situated mainly at the harzburgite/dunite junction and occurs as discontinuous layers that occasionally were large enough to be economically extractable. The largest concentrations of chromitite were at Kokkinorotsos mine, from which at least 0.5 million tons of chromitite have been extracted (Greenbaum, 1977) (Fig.2). The chromite nodules studied here are from two localities just west of Kokkinorotsos on Mt Olympus, (chromite occurrences 2 and 3, Fig. 2) where the best orbicular, nodular and skeletal chromites were first described by Greenbaum (1977) and

140 further studied by Leblanc (1980).

141

142 **2. Methods**

143

144 Two samples of nodular chromite containing skeletal chromites were selected for 3D imaging.
145 Cores of 25 mm diameter were drilled into the nodular chromite. These cores were scanned using
146 the XRADIA XRM 500 high-resolution 3D X-ray microscope system at the Australian Resources
147 Research Centre (ARRC, Kensington, Western Australia). The scanner was set-up to 160 kvV
148 voltage, 10 W power and a voxel size of 13 µm. A total of 2000 projections were recorded over
149 360° for each sample and were used to reconstruct the 3-D volumes. The generated data were
150 processed and analysed using AvizoFire® and CSIRO-developed codes, following methods
151 described by Godel (2013). One core was subsequently cut and polished down to a particular slice
152 where the geometric centre of a skeletal crystal-cored nodule had been located in the 3D scan. This
153 area was selected for electron backscatter diffraction (EBSD) analysis. The sample surface was
154 prepared for EBSD via chemical-mechanical polishing (CMP) using colloidal silica (Prior et al.
155 1999, Halfpenny, 2010; Halfpenny et al., 2013) and given a thin carbon coat to prevent charging in
156 the SEM. EBSD data were collected from two systems. Large area simultaneous EBSD and EDS
157 mapping of a single nodule was undertaken using Tescan Mira3 field emission SEM, housed in the
158 Electron Microscopy Facility at Curtin University, Perth, using an accelerating voltage of 20kV and
159 probe current of 17nA. EBSD data were collected by a NordlysNano EBSD detector, whilst EDS
160 data were collected on a X-Max 150 silicon drift detector. Data were acquired using the automatic
161 mapping capability of Oxford AZtec 2.2 Full crystallographic orientation data from individual
162 chromite grains were obtained also from automatically indexed Kikuchi diffraction patterns
163 collected using a Bruker e$^-$flash detector fitted on a Zeiss Ultraplus FEG SEM at the CSIRO
164 facilities, Kensington, Western Australia. Coincident energy dispersive X-ray spectra (EDS) were
165 collected with a Bruker XFlash 5030 silicon drift EDS detector and this information was used to

accurately separate the phases. This SEM was operated using an accelerating voltage of 20kV, a 120µm aperture, in high current mode which produced a beam current of 12.1nA. The EBSD data were collected using the Bruker Quantax Espirit 1.9 software, using a resolution of 200x150 pixels, a 11.5ms exposure time and a step size of 5.12µm (determined by the size of the smallest grain of interest). All EBSD data were post-processed using Oxford Instruments Channel 5 software to remove mis-indexed points and interpolate non-indexed points (Prior et al., 2009). The corrected data files were then used to generate the presented EBSD images. Chromite analyses were performed using a Cambridge Instruments (ZEISS NTS) S360 scanning electron microscope (SEM), coupled to an Oxford Instruments INCA energy plus which included both an energy dispersive (ED) and a wave dispersive (WD) X-ray analytical system at Cardiff University. Chromite single point analyses were performed also with a 20kV accelerating voltage, 20 nA beam current and fixed beam size (approximately 10-15 nm) with a live-time of 50 s for ED. A cobalt standard and separate chromite standard were used to monitor for instrumental drift. X-ray fluorescence mapping was carried out using a Bruker Tornado desktop X-ray microscope at CSIRO, Perth, equipped with silicon drift detector operating at count rates of about 100-150 kcps, x-ray tube conditions 50 kV, 600 microamps, spot size 25 microns, 25 micron step size, x-ray energy resolution less than 145 eV. Results were ZAF corrected and presented as element concentration maps using native Bruker software.

3. Results

3.1 Nodules and skeletal crystals in 2D

Samples were collected from locality 2 (Fig. 2) where there are dunites containing nodular and skeletal chromite. Layers of nodules contain skeletal chromite growths both in their cores and between nodules. The skeletal crystals are particularly common at the edges of the layers of nodules

192 (Figs. 3A, and 4) and there are more skeletal chromites in the adjacent dunite (Fig. 3A).

193

194 Figure 3 here

195

196 The nodules are approximately 1 cm in diameter and are round, oval and sometimes triangular with
197 rounded corners. The skeletal chromites may be up to 5-6 cm across (Fig. 3B) and consist of
198 elongate blades of chromite with branches on each side. There are also triangular sections of
199 chromite with equi-dimensional sides (Fig. 3B1).

200

201 The orbicular chromitite consists of layers of chromite that appear to be draped around irregular
202 cores of dunite (Fig. 3 C and D). In one case a chromite triangle with cross bars of chromite occurs
203 with the skeletal chromites (Fig. 3E1) and in another a chromite nodule partially surrounds a
204 triangle structure with cross bars of chromite (Fig. 3F). The nodules containing skeletal chromites
205 enclose serpentinised olivine, clinopyroxene (now clinochlore) and plagioclase whereas the nodules
206 and skeletal crystals are surrounded only by serpentinised olivine. No sulfide or PGM phases such
207 as laurite or OsIrRu alloys were observed in these samples. Sulphur saturation and precipitation of
208 Pt- and Pd-bearing PGM did not occur in Cyprus until higher in the stratigraphy in the gabbro
209 (Prichard and Lord, 1990).

210

211 Figure 4 here

212

213 Cores from two samples from location 2 (Fig. 2) containing nodular chromite have been chosen for
214 3D imaging; ND 7 (Fig 4A) and ND 16 (Fig. 4B). The ND 7 core consists of nodular chromite
215 containing skeletal centres. Skeletal chromite occurs between these nodules (Fig. 4A). ND 16
216 consists of nodular chromite enclosing skeletal chromite but with less interstitial skeletal chromite.
217 The ND16 core is taken from a layer of nodular chromite. On the edge of this layer of nodules is

skeletal chromite with no rim of chromite surrounding it (Fig. 4B, #1). In the first row of chromite nodules along the edge of the nodular layer the skeletal chromite is totally (Fig. 4B#2) or partially (Fig. 4B#3) surrounded by a thin rim of chromite and further towards the centre of the layer of nodular chromite the skeletal chromite is completely surrounded by a thick rim of chromite (Fig. 4B#4). This progression of textures from the edge towards the centre of the nodule layer suggests that the skeletal crystals formed first and then the outer rim of chromite formed around them. ND 16 displays a variety of nodule shapes including those that are more angular than rounded. The outline of the skeletal chromite that forms the core of the nodule is reflected in the form of the outer nodule shell, and this gives rise to irregular shaped nodules; for example the rectangular nodule with rounded corners (located within the black square, Fig. 4B).

3.2 Nodules and skeletal crystals in 3D

High-resolution X-ray computed tomography (CT) provides 3D visualization of nodule structures and their core skeletal crystals. The CT data allow images to be examined in any chosen orientation, at 13 micron resolution throughout the volume of the sample analysed. Circular images (Fig. 5) across the core (Fig. 4A), chosen from 1043slices through this core, illustrate the textures of the skeletal and nodular chromite. The nodules and interstitial skeletal shapes of the chromite are clearly displayed and these are placed in context in the text that describes Fig. 9.

Figures 5 and 6 here

Silicates, including clinochlore, tremolite-actinolite and serpentine, are located between the skeletal chromite blades and are commonly completely enclosed by the nodule and isolated from the serpentine surrounding the nodule. It is also the case that silicates are trapped as inclusions between branches of skeletal chromite interstitial to the chromite nodules and are also isolated from the

surrounding silicate matrix, composed of serpentine after original olivine (Fig. 5).

The branches of chromite in skeletal crystals can be observed in 3D to extend to form a series of parallel sheets (Fig. 6A). In 3D it is clear that the nodules usually touch one another and they may also be interconnected with the interstitial skeletal chromite (Figs. 6B and D). Isolated octahedra of chromite are also present between the chromite nodules (Fig. 6C).

3.3 Electron Backscatter Diffraction (EBSD)

A nodule containing skeletal chromite surrounded by a chromite rim, from the core that was scanned using 3D X-ray tomography from sample ND 16, was selected for more detailed study. Sections taken at right angles through the long axis of this nodule show a skeletal texture and a double Y shape in the orthogonal section (Fig. 7A-C). The skeletal crystals are enclosed by a chromite rim draping around the skeletal crystals and mimicking the shape of the outer surfaces of the skeletal crystals (Figs. 4B and 7A-C).

Orientation mapping of the nodule reveals a core of skeletal crystals surrounded by grains up to ~1mm in diameter that form a discrete rim around the core (Fig. 7D). The skeletal core displays a much smaller range of orientations than the polycrystalline chromite grains in the rim (Fig. 7D). Internally, the skeletal core records a limited range of orientations (Fig. 7D, F, G) but records lattice distortions accommodated by discrete low-angle boundaries as well as a more subtle substructure (Fig. 7D and E). In contrast, the rim grains tend to show smaller degrees of lattice distortion (Fig. 7D and E), although this is spatially quite heterogeneous (Fig. 7E, 8A-C), being preferentially developed where the chromite grains impinge on a neighbouring nodule (Fig. 8C). The relationship between the core and rim grains is also complex with most rim grains commonly showing misorientation angles of 10-20° with adjacent parts of the core. However, a few grains show misorientations as large as ~60°. These grains record a common {110} pole to the host (Fig. 7F and

G). The distribution of misorientation angles within the nodule indicates that therim grains are not randomly-oriented with respect to the host, further indicating a crystallographic relationship between host and rim grains.

Figure 7 here

Figure 8 here

Chromite grains that make up the polycrystalline rim exhibit generally a smooth, but in detail crenulated, outer edge. Grain boundaries between the chromite grains in the rim are clearly truncated on the outer edge of the rim (e.g. Fig. 8A-D). Grain-scale microtextures within the rim range from random growth impingement with curved grain boundaries to well-developed adcumulate textures with equilibrium 120 degree grain boundaries (Fig. 7 D and E).

3.4. Chemical variability within the nodule

The chromite within the skeletal crystal and outer polycrystalline rim of the nodule analysed by point analyses (Fig. 8 D) and also mapped by energy dispersive spectrometry (EDS) in the course of the EBSD mapping shows that the chromite compositions across the entire nodule are remarkably similar throughout. SEM (EDS) element concentration maps for the selected sample are shown in Figs. 8 E and F. This indicates that the chromite aggregates are homogenous at a 50 micron scale within the precision of the analyses (plus or minus about 2% in FeO and Cr_2O_3) and that there is no detectable chemical zoning across the nodules.

The very edges of individual grains in the chromite rim are altered to a more Fe-rich and Mg- and Al-poor chromite. This alteration is common on the edges of all the grains in the rim of the nodule

296 (Fig. 8D, Table 1) and allows identification of the outlines of other grains in the rim as imaged by
297 EBSD (Fig. 7 D and E). This feature also allows grain boundaries in granular rims to be identified
298 in other nodules.
299
300 Table 1 here
301
302 The nodules are embedded in a matrix of olivine now altered to serpentine, the only other visible
303 phase being Al-rich chlorite and a Ca-rich tremolite amphibole developed within the core of the
304 prominent skeletal crystal-cored nodule (Fig. 8 E and F). This phase is interpreted as the product of
305 alteration of the Ca and Al-bearing component of silicate melt trapped within the core framework.
306
307 **4. Discussion**
308
309 *4.1 Formation of hopper crystals*
310
311 The skeletal crystals show different stages of growth initially with just a few joined blades of
312 chromite to more complete forms where blades are linked together enclosing silicates. In rapid
313 crystallisation it is generally accepted that a crystallising component is added more quickly at
314 crystal edges rather than in the centre of a crystal plane. In skeletal growth, fast growing facets
315 extend through the depleted chemical boundary layer that forms around the growing skeletal
316 crystal; in this way the fast-growth facets can continue to develop from undepleted solute, while
317 other less favourable oriented facets have their growth inhibited by being starved of supply of their
318 growth components. The resulting crystals are hopper shaped and are characterised by fully
319 developed crystal edges with hollow interiors. Partially formed hopper crystals consist of complex
320 intergrowths of formations (Fig. 9). A complete hopper crystal is also sometimes known as a
321 skeletal cube (Phillips, 1965). Hopper crystals are commonly developed in crystals such as halite

322 and native bismuth. In 3D the Troodos skeletal crystals form hopper crystals and on 2D surfaces the
323 great variety of shapes correspond to sections across the hopper crystals.
324
325 Partially formed hopper crystals display complex growths that contain 3D arrow head structures
326 (Figs. 9 A and B). The fully formed hopper crystals consist of complete boxes where the arrow
327 heads have grown into cubes (Fig. 9 C). The 2D images of the skeletal crystals, both enclosed and
328 interstitial to chromite nodules, show a diversity of cross sections of hopper forms, with some of the
329 rarer forms including chromite triangles (Figs. 3B1, 5D2, 6D, 9J) with arrow shaped corners (Fig.
330 5B1), triangles containing partial (Fig. 5D1 also shown in 9F) or complete parallel blades linking
331 two sides of the triangle (Fig. 3E also shown in 9H) and a double Y shape (> −<) (Figs. 4C, 5C1,
332 7B and 9E and J). The 3D images of the skeletal crystals, both within and interstitial to the nodules,
333 show that they are actually formed of cages with hopper structures. It is also apparent that the
334 cage/hopper crystals are not always complete often having been in the process of growth as
335 crystallisation ceased (Figure 9D). Thus the arrow head textures and the triangles with partially
336 formed blades of chromite observed in 2D may be ascribed to partially formed cage/hopper crystals
337 (Figs. 9 E and F). The triangular chromite with skeletal parallel lines (Fig. 3F) is very similar to the
338 partially formed hopper crystal shown in Fig. 9B.
339
340 EBSD data show that the skeletal crystals recorded in the core of a nodule crystallise in a similar
341 orientation yet record a significant component of lattice distortion (Fig 7D-G). These variations in
342 orientation may be deformation-related features, related to late stages of solidification as noted for
343 zircon grains in andesite-derived cumulates (Reddy et al 2009). However, the lattice distortion is
344 greater than that recorded in rim grains and is therefore unlikely to represent only the effects of
345 post-rim deformation. More likely is that a component of the distortion represents the incorporation
346 of defects during growth of the hopper crystals. Such growth is widely recognised in non-geological
347 materials (e.g. Tiller 1991) and has been observed recently by EBSD in minerals crystallising from

melts and fluids (McLaren & Reddy 2008; Timms et al 2009).

The skeletal chromites studied here appear to be elongate cage/hopper crystals (Figs. 7A and 9). The characteristic solid angle between the crystal faces shows that this skeletal core grew by preferential development of <111> facets (Figs. 7F-G and 9G). This is consistent with the orientation of dominant facets reported for dendritic chromite in komatiites by Godel et al. (2013).

Figure 9 here

As the skeletal crystals grow they joined up to form the cage/hopper structure illustrated in Fig 9G. Cross sections such as observed in Fig. 3E (Fig. 9H), the almost complete double Y shape observed in Fig. 5C (Fig. 9J), and the skeletal branching structure (Fig. 9K) can be explained as sections across a complete or almost complete cage/hopper crystal.

4.2 *Origin of Troodos skeletal-cored chromite nodules*

Greenbaum (1977) concluded that the skeletal crystals in the centres of the chromite nodules from Troodos, formed from supersaturation and /or supercooling of a magma and that there was a continuous growth from skeletal crystals to massive nodules. Greenbaum (1977) did not comment specifically on the conditions needed for the formation of the rim to the skeletal crystals. He interpreted orbicular chromite as mechanical accretion of previously settled chromite grains around a nucleus of dunite.

Leblanc (1980) re-examined these nodular and skeletal chromites from Troodos and agreed that there was a sequence of textures from skeletal crystals with octahedral terminations and lamellae (111) from initial Christmas tree forms becoming progressively in filled to form rounded nodules.

374 Euhedral terminations have the form (100), (110), (111) and (100). He concluded that the rounded
375 surfaces are due to dissolution processes taking place in an open space moving environment.
376
377 *4.3 Observations from the 3D study of these Troodos nodules*
378
379 The results presented here broadly support the conclusions reached by Greenbaum (1977) and
380 Leblanc (1980) using 2D observations. Interpretation of the 3D images corroborates the idea that
381 these nodules formed by overgrowth of polycrystalline equant chromite aggregates onto pre-
382 existing cores of skeletal chromite. The external shape of the nodule is determined by the shape of
383 the accretion of the chromite rim draping over the skeletal crystal core. This gives the nodule either
384 a spherical or a less regular more cubic shape but with rounded outer surfaces caused by the
385 truncation of the granular rim. This demonstrates that the nodules grew from the centre outwards.
386 There is no change in the composition of the chromite from the skeletal crystal outwards to the rim
387 (Fig. 8 D, E and F) although it is possible that any such changes may have been lost due to later re-
388 equilibration of the chromite.
389
390 A key observation in this study is that the grain orientations of the overgrown chromite rim are not
391 random, but inherit a similar crystallographic orientation to that of the core skeletal crystal (Fig. 7).
392 In cases where misorientation relationships between core and rim are large (~60°), the core and
393 rim share a common {210} pole, further supporting a close crystallographic relationship between
394 core and rim crystallography. This has an important implication: the rim accretion process is not
395 mechanical, as this would produce random grain orientations, but rather is the consequence of
396 heterogeneous nucleation of rim grains on the original skeletal crystal substrate. This has
397 ramifications for current models of nodule formation, as discussed below.
398
399 The 3D images elucidate the growth history and explain the different chromite morphologies.

Initially skeletal chromite growth, driven by rapid crystallisation from Cr-supersaturated magma, forms elongate blades with <111> facets that nucleate side <111> branching out from the central blade (Fig. 10A). As growth proceeds the tips of the fastest growing branches extend through the depleted boundary layer around the rapidly growing skeletal crystal, and the tips spread sideways to form arrow shapes that in 3D appear as octahedral pyramids (Fig. 10B and Fig. 5C). In 3D the elongate skeletal growths often form a double Y shaped spine; as growth continues side plates from this double Y shaped spine grow and join, resulting in a cage structure rather than a branching structure. The growth of the side plates to join with the octahedral tips produces hopper structures on the faces of the cage (Fig.9).

As the degree of supersaturation in Cr decreases, skeletal growth ceases and further chromite growth takes place by heterogeneous nucleation of new grains on the skeletal chromite, followed by non-skeletal homogenous growth. A polycrystalline rim begins to form around the skeletal core, the growing equant crystals impinge to form curved non-faceted grain boundaries. Eventually a complete rim develops that encloses the skeletal crystal while mimicking its original external outline (Fig. 10C and C).

The EBSD data show that this nodule rim is made up of multiple crystals with rounded edges; these crystals grew adjacent to each other to form the coating around the skeletal grain. The undulatory outer surface of the nodule truncates grain boundaries of chromite grains in the rim, all the way around the entire nodule, and planar crystal facets are absent on the outer surface of the nodule. This suggests mechanical abrasion or partial dissolution of the nodule subsequent to crystallisation of the polycrystalline rim (Fig. 10D). This supports the idea of Leblanc (1980) that the smooth edge of the nodule is formed by dissolution and the observation that the nodules appear corroded (Thayer, 1964).

426 The EBSD data further show deformation of the chromite grains in the rim where nodules touch
427 indicating that the nodules impinged on one another before the surrounding matrix to the nodules
428 was completely solid, and after the truncation episode which we interpret as having happened while
429 the nodules were still suspended in magma. The impingement could have occurred by transient
430 collision as nodules settled, or during compaction and deformation of the nodule layer following
431 accumulation of the nodule layer.
432
433 Figure 10 here
434
435 *4.4 Evidence for quiescent conditions during nodule formation*
436
437 The erosion of the outer surface of the nodule has been interpreted as the result of mechanical
438 abrasion in a rapid flowing magma during formation as suggested by a number of authors (e.g
439 Moghadam et al., 2009). Outcrops of nodular chromite may also display frozen flow structures
440 interpreted as indicating rapid flow conditions (Huang et al., 2004). However this could equally
441 well result from dissolution prior to consolidation. Barnes (1986) shows images of scalloped edges
442 on chromite grains that had been heated experimentally above the liquidus of the enclosing melt
443 and had undergone partial dissolution. The geometry is broadly similar to that of the nodule
444 surfaces. The EBSD data (Fig. 8) indicate truncation of grains resulting in a smooth edge to the
445 nodule but in detail this smooth surface is pitted or scalloped resulting from two stages of
446 dissolution. It seems unlikely that the truncation is caused by erosion of the nodules in a rapidly
447 flowing magma because the skeletal crystals external to the nodules are not broken and damaged.
448 They would be so if the movement was sufficient to round and truncate the nodules. Indeed 3D
449 imaging has shown that the skeletal crystals external to the nodules are commonly attached to the
450 nodules. Partially formed hopper crystals could be preserved as they were forming or they may have
451 been more complete and then subjected to dissolution.

This all mitigates against a change from quiescent to rapidly moving magma during the formation of skeletal crystals and then nodules, rather it supports the idea that the change from skeletal chromite formation to nodule formation is due to a change from supersaturation of the magma to one of crystallisation at equilibrium close to the liquidus, followed by dissolution in an environment of chromite undersaturation.

A previously suggested analogue for the formation of chromite nodules is the growth of sedimentary ooliths around irregular core fragments in as they roll in currents as is suggested for chromite nodules (Ahmed, 1982; Lago et al., 1982; Lorand and Ceuleneer, 1989; Thayer, 1969 and Dickey 1975). We are suggesting here that the skeletal crystals served as the original nuclei onto which the nodular chromite grew. A possibly more apposite analogy is the formation of graupel, which is soft hail or snow pellets formed from super cooled droplets freezing onto snowflakes, as described in Pinsky et al. (1998). Graupel grains attach to snowflakes producing a collection of grains that make up a rim around the skeletal snowflake. This is very similar to the texture observed in the Troodos nodules (Fig. 11).

Figure 11 here

4.5. Implications for in-situ adcumulus growth

An interesting feature of the granular chromite rim is that portions of it have evidently developed with equilibrium adcumulate textures with 120 degree triple point boundaries (Fig. 7 D). These textures are commonly interpreted in classical cumulus theory as forming due to annealing by filter pressing of trapped intercumulus liquid. However, this mechanism is clearly inapplicable here. An alternative mechanism involving in-situ growth of an adcumulate crust at the crystal liquid interface

478 has been proposed for the Jimberlana adcumulate, (Campbell, 1977; Campbell, 1987) and has been
479 demonstrated experimentally by Lesher and Walker (1988). The textures exhibited in the nodule rim
480 constitute observational evidence for this hypothesis. The alternative explanation is that the rims
481 have undergone recrystallisation and annealing, but this is inconsistent with the preservation of
482 highly disequilibrium skeletal crystal in the core. We interpret the adcumulus rim aggregates as the
483 result of highly efficient textural equilibration during near-liquidus growth of chromite in a well-
484 mixed, well stirred medium where boundary layers around the growing chromite grains were
485 disrupted by shear flow between the magma and the growing nodule, analogous to the in situ
486 growth of olivine adcumulates at the base of flowing komatiite lavas (Godel et al 2013).
487
488 *4.6. Implications for petrogenesis of nodular chromitite*
489
490 Matveev and Ballhaus (2002) have proposed an elegant and self-consistent model for the origin of
491 podiform chromitite based on physical collection of dispersed chromite grains by ascending vapour
492 bubbles within a water saturated boninite melt. Our observations in relation to their model are
493 somewhat equivocal. On one hand, sudden devolatilisation of a water-oversaturated magma
494 provides a mechanism for constitutional supercooling following a sudden pressure drop, and this
495 could provide an appealing mechanism for the initial formation of the skeletal crystal. On the other
496 hand, the spherically symmetrical deposition of skeletal and granular chromite in our nodule is hard
497 to reconcile with what would be an essentially stochastic process of mechanical entrainment of
498 chromite grains during bubble ascent; a random spatial disposition of grain shapes and sizes would
499 be expected within the nodule from what is purely a mechanical collection process. Our obser-
500 vations are more consistent with sequential growth. Specifically, the preferential orientation of
501 the granular rim grain population towards the crystallographic orientation of the skeletal crystal
502 (Fig.7) argues strongly for a heterogeneous nucleation control rather than purely chance physical
503 agglomeration. The presence of localised patches of adcumulate texture within the rim has the
same

implication. Furthermore, our observations attest to a post-growth dissolution mechanism to produce the rounded outer surface of the nodule, which in the Matveev and Ballhaus model is attributed to the surface tension-controlled outer surface of the entraining moving bubble. Our observations suggest a general lack of movement during nodular rim formation. While our observations do not disprove the bubble-collection hypothesis, they strongly favour a mechanism of accretionary growth.

5. Conclusions

A combination of microcharacterisation techniques on spectacular samples of skeletal-cored chromite nodules provides new insights into crystallisation mechanisms. The key observations are:

1) the skeletal core is a single crystal, formed by rapid preferential growth of <111>facets, as observed in skeletal chromites from other settings;

2) the core is surrounded by a polycrystalline rim showing non-random crystallographic relationships to the host skeletal crystal core implying that the rim formed by accretionary crystal growth, and not by mechanical agglomeration;

3) the nodule rim contains domains of adcumulate texture implying that such textures can form as primary crystallisation features and do not require mechanisms such as trapped liquid expulsion; further, adcumulate textures in chromitites do not require recrystallization, but can be the direct result of primary crystallisation from the magma at its liquidus;

4) grain boundaries in this rim are truncated by an undulose outer surface on the nodule that was predominantly formed by dissolution of the nodule after incorporation into chromite undersaturated magma;

5) minor deformation of the nodule occurred at a late stage, preferentially at impingement points with neighbours.

The evidence presented here implies that skeletal chromite cores to nodules from the Troodos ophiolite formed first and were then coated with individual chromite grains, indicating that the nodules grew from the centre outwards. As observed in 3D the skeletal crystals are likely to have grown rapidly along preferred fast-growing crystallographic directions in a regime of chromite supersaturation, forming blades of chromite that produce a cage/hopper structure elongated along <111>. Then, as the degree of supersaturation decreased, the rate of chromite nucleation increased relative to the rate of growth, and multiple individual grains formed around the skeletal crystals. These aggregated to produce a rim that retains the overall geometric outline of the skeletal crystal. This accounts for the crystal-like morphology of the entire polycrystalline nodule. Truncation of the grains on the edge of the rim suggests that the nodules were subsequently partially dissolved, in a chromite undersaturated magma. Then at some point post formation the nodules collided and were deformed at impingement points.

The disposition of crystal shapes and orientations in the nodule is considered to be inconsistent with a process of mechanical collection of pre-existing chromite grains by vapour bubbles. The observed textures record sequential crystallisation of a suspended crystal aggregate under varying degrees of chromite saturation. The progression from skeletal crystals in the core to equant polycrystalline rim to subsequent resorption records a growth sequence influenced by changing chemical environments: initial growth from chromite-supersaturated magma allowed skeletal crystal growth, followed by breakdown of chemical boundary layers giving rise to granular growth in preferred orientations and in local textural equilibrium. Subsequent incorporation of the nodule into chromite undersaturated magma gave rise to dissolution and truncation of pre-existing grain boundaries atthe edge of the nodule rim.

Nodular chromite without skeletal cores is commonly described from ophiolite complexes. The growth of these Cypriot nodules by accumulation of granular chromite to form polygranular rims

around a skeletal nucleus may be a more widespread process in the formation of the more common types of nodular chromite which do not preserve visual evidence of skeletal crystals in their cores but may have formed in a similar way by growth around a nucleus. The observations described here, made possible by the use of 3D tomography and EBSD, may also point to a key link in the understanding of the process of podiform chromitite formation in ophiolites in general. The formation of the chromite nodules suggests that the magma fluctuates from Cr oversaturated to under saturated and may indicate that chromitite in ophiolite complexes forms in a regime that oscillates from supersaturated, supercooled conditions to conditions of chromite undersaturation Our observations attest to the formation of chromite nodules in a magmatic environment of fluctuating cooling rate and magma composition.

Acknowledgements

Hazel Prichard would like to thank the CSIRO Office of the Chief Executive (OCE) for funding this research during a Distinguished Visiting Fellowship. Angela Halfpenny is funded by the CSIRO OCE Postdoctoral Fellowship scheme. Zoja Vukmanovic and Steve Reddy acknowledge support through the Australian Research Council Core to Crust Fluid Systems Centre of Excellence and ARC LIEF Funding. Mark Pearce is thanked for contributing to the interpretation of the EBSD images, and along with Patrick Nadoll for a very thorough review of an early draft. This is an output of the CSIRO Minerals Down Under National Research Flagship.

References

Ahmed, Z., 1982. Porphyritic-nodular, nodular, and orbicular chrome ores from the Sakhakot-Qila complex, Pakistan, and their chemical variations. Mineralogical Magazine 45, 167-178.

582 Ahmed, A.H., Arai, S., Attia, A.K., 2001. Petrological characteristics of podiform chromitites and
583 associated peridotites of the Pan African Proterozoic ophiolite complexes Egypt. Mineralium
584 Deposita 36, 72-84.
585
586 Arai, S., Yurimoto, H., 1994. Podiform chromitites of the Tari-Misaka ultramafic complex,
587 southwestern Japan, as mantle-melt interaction products. Economic Geology 89, 1279-1288.
588
589 Ballhaus, C., 1998. Origin of podiform chromite deposits by magma mingling. Earth and Planetary
590 Science Letters 156, 185-193.
591
592 Barnes, S.J., 1986. The distribution of chromium among orthopyroxene, spinel and silicate liquid at
593 atmospheric pressure: Geochimica et Cosmochimica Acta. 50, 1889-1909.
594
595 Brown, M., 1980. Textural and geochemical evidence for the origin of' some chromite deposits in
596 the Oman ophiolite, in: Panayiotou, A., (Ed.), Ophiolites. Proceedings of the International Ophiolite
597 Symposium, Cyprus, pp. 714-721.
598
599 Campbell, I.H., 1977. A study of macrorhythmic layering and cumulate processes in the Jimberlana
600 Intrusion, Western Australia, Part I: The upper layered series. J. Petrol. 18, 183-215.
601
602 Campbell, I.H., 1987. Distribution of orthocumulate textures in the Jimberlana Intrusion. J. Geol.
603 95, 35-54.
604
605 Ceuleneer, G., Nicolas, A., 1985. Structures in podiform chromite from the Maqsad District (Sumail
606 Ophiolite, Oman). Mineralium Deposita 20, 177-185.
607

608 Christiansen, F.G., Olesen, N.O., 1990. Large skeletal chromites in the Vourinos ophiolite, Greece.
609 Bulletin of the Geological Society of Denmark 38, 33-42.
610
611 Dickey, J.S.Jr., 1975. A hypothesis of origin for podiform chromite deposits. Geochimica
612 Cosmochimica Acta, 39, 1061-1074.
613
614 Dilek, Y., 2003. Ophiolite concept and its evolution, in: Dilek, Y., Newcomb, S., (Eds.), Ophiolite
615 Concept and the Evolution of Geological Thought, Geological Society of America Special Paper
616 373, pp. 1–16.
617
618 Dowling, S.E., Barnes, S.J., Hill, R.E.T., Hicks, J., 2004. Komatiites and Nickel Sulphide Ores of
619 the Black Swan area, Yilgarn Craton, Western Australia. 2. Geology and Genesis of the Orebodies.
620 Mineralium Deposita 39, 707-728.
621
622 Economou-Eliopoulos, M., 1996. PGE distribution in chromite ores from ophiolite complexes:
623 implications for their exploration. Ore Geology Reviews 11, 363-381.
624
625 Godel, B., 2013. High-resolution X-ray computed tomography and its application to ore deposits:
626 from data acquisition to quantitative three-dimensional measurements with case studies from Ni-
627 Cu-PGE deposits; Economic Geology 108, 2005-2019.
628
629 Godel, B., Barnes, S.J., Gurer, D., Austin, P. Fiorentini, M.L., 2013. Chromite in komatiites: 3D
630 morphologies with implications for crystallization mechanisms. Contributions to Mineralogy and
631 Petrology 165, 173-189.
632
633 Golding, H.G., 1975. Relict textures of chromitites from New South Wales. Journal of the

634 Geologial Society of Australia 22, 397-412.
635
636 González-Jiménez, J. M., Griffin, W. L., Proenza, A., Gervilla, F., O'Reilly S. Y., Akbulut, M.,
637 Pearson, N. J., Arai, S., 2014. Chromitites in ophiolites: How, where,when, why? Part II. The
638 crystallisation of chromitites. Lithos 190-191, 520- in press.
639
640 Greenbaum, D., 1977. The Chromitiferous rocks of the Troodos ophiolite, Cyprus. Economic
641 Geology 72, 1175-1194.
642
643 Groves, D.I., Barrett, F.M., Binns, R.A., McQueen, K.G., 1977. Spinel phases associated with
644 metamorphosed volcanic-type iron–nickel sulphide ores from Western Australia. Economic
645 Geology 72, 1224–1244.
646
647 Halfpenny, A., 2010. Some important practical issues for collection and manipulation of electron
648 backscatter diffraction (EBSD) data from rocks and minerals. Journal of the Virtual Explorer 35, 1-
649 18.
650
651 Halfpenny, A., Hough, R.M., Verrall, M., 2013. Preparation of samples with both hard and soft
652 phases for electron backscatter diffraction: Examples from gold mineralisation. Microscopy and
653 Microanalysis 19, 1007-1018.
654
655 Huang, X., Li, J., Kusky, T.M., Chen, Z., 2004. Microstructures of the Zunhua 2.50 Ga podiform
656 chromite, North China Craton and implications for the deformation and rheology of the Archaean
657 oceanic lithospheric mantle, in: Kusky, T.M., (Ed.) Precambrian ophiolites and related rocks,
658 Developments in Precambrian geology Chapter 10, 13 (K C Condie series Ed.) pp. 321-337.
659

660 Irvine, T.N., 1977. Origin of chromitite layers in the Muskox intrusion and other stratiform
661 intrusions: A new interpretation. Geology 5, 273–7.
662
663 Jackson, E.D., 1969. Chemical variation in coexisting chromite and olivine in chromitite zone of the
664 Stillwater Complex, in Wilson H.D.B. (Ed.), Magmatic Ore Deposit Economic Geology
665 Monograph 4, 41– 71.
666
667 Keleman, P.B., 1995. Extraction of mid-ocean ridge basalt from the upwelling mantle by focused
668 flow of melt in dunite channels. Nature 375, 747-753.
669
670 Lago, B.L., Rabinowicz, M., Nicolas, A., 1982. Podiform chromite orebodies: a genetic model.
671 Journal Petrology 23, 103-125.
672
673 Leblanc, M., 1980. Chromite growth, dissolution and deformation from a morphological view
674 point: SEM investigations. Mineralium Deposita 15, 201-210.
675
676 Leblanc, M., Ceuleneer, G., 1992. Chromite crystallization in a multicellular magma flow:Evidence
677 from a chromitite dike in the Oman ophiolite. Lithos 27, 231-257.
678
679 Lesher, C.E., Walker, D., 1988. Cumulate maturation and melt migration in a temperature gradient.
680 J. Geophys. Res. 93B, 10295-10311.
681
682 Lorand, J.P., Ceuleneer, G., 1989. Silicate and base-metal sulphide inclusions in chromites from the
683 Maqsad area (Oman ophiolite, Gulf of Oman): A model for entrapment. Lithos 22, 173-190.
684
685 Naldrett, A.J., Kinnaird, J.A., Wilson, A., Yudovskaya, M.A., McQuade, S., Chunnett, G., Stanley,

686 C., 2009. Chromite composition and PGE content of Bushveld chromitites: Part 1 - the Lower and
687 Middle Groups. Transactions of the Institute Mining and Metallurgy B 118, 131-161.
688
689 Matveev, S., Ballhaus, C., 2002. Role of water in the origin of podiform chromitite deposits: Earth
690 and Planetary Science Letters 203, 235–243.
691
692 Sandra McLaren, S., Reddy, S. M., 2008. Automated mapping of K-feldspar by electron backscatter
693 diffraction and application to 40Ar/39Ar dating:Journal of Structural Geology 30, 1229–1241.
694
695 Melcher, F., Grum, W., Simon, G., Thalhammer, V.T., Stumpfl E.F., 1997. Petrogenesis of the
696 ophiolitic giant chromite deposits of Kempirsai, Kazakhstan: a study of solid and fluid inclusions in
697 chromite. Journal of Petrology 38, 1419–1458.
698
699 Moghadam, H.S., Rahgoshay, M., Forouzesh, V., 2009. Geocheomical investigation of nodular
700 chromites in the Forumad ophiolite, NE of Iran. Iranian Journal of Science and Technology,
701 Transactions A 33,103-108.
702
703 Morishita, T., Andal, E.S., Arai, S., Shida, V.I., 2006. Podiform chromitites in the lherzolite-
704 dominant mantle section of the Isabela ophiolite, the Philippines. Island Arc 15**,** 84–101.
705
706 Pagé, P., Barnes, S-J., 2009. Using trace elements in chromites to constrain the origin of podiform
707 chromitites in the Thetford Mines ophiolite, Québec, Canada. Economic Geology 104, 997–1018.
708
709 Paktunc, A.D., 1990. Origin of podiform chromite deposits by multistage melting, melt segregation
710 and magma mixing in the upper mantle. Ore Geology Reviews 5, 211-222.
711

712 Pavlov, N.V., Grigoryeva, I., Tsepin, A.I., 1977. Chromite nodules as an indicator of liquation of a
713 magmatic melt: International Geology Reviews 19, 43-56.
714
715 Phillips, F. C., 1971. An introduction to crystallography, fourth ed.. Oliver and Boyd, Edinburgh.
716
717 Pinsky, M., Khain, A., Rosenfeld, D., Pokrovsky, A., 1998. Comparison of collision velocity
718 differences of drops and graupel particles in a very turbulent cloud: Atmospheric Research 49, 99-
719 113.
720
721 Prior, D.J., Boyle, A. P., Brenker, F., Cheadle, M. C., Day, A., et al., 1999. The application of
722 electron backscatter diffraction and orientation contrast imaging in the SEM to textural problems in
723 rocks. American Mineralogist 84, 11-12,1741-1759.
724
725 Prior, D.J., Mariani, E., Wheeler, J., 2009. EBSD in the earth sciences: applications, common
726 practice and challenges, in Schwartz, A.J., Kumar, M., Adams, B.L., Field, D.P., (Ed.), Electron
727 Backscatter Diffraction in Materials Science, Berlin, Springer, 345-360.
728
729 Prichard, H.M., Neary, C.R., 1982. Some observations on the chromite in the Shetland
730 ophiolite complex. Ofioliti 2/3, 455-466.
731
732 Prichard, H.M., Lord, R.A., 1990. Platinum and palladium in the Troodos ophiolite complex,
733 Cyprus. Canadian Mineralogist 28, 607-617.
734
735 Prichard, H.M., Brough, C., 2009. Potential of ophiolite complexes to host PGE deposits. In New
736 developments in magmatic Ni-Cu and PGE deposits, in: Li, C., Ripley E.M. (Eds.) Geological
737 publishing house Beijing, pp. 277-290.

738

739 Proenza, J., Gervilla, F., Melgarejo, J.C., Bodinier. J. L., 1999. A1-and Cr-Rich chromitites from the
740 Mayari-Baracoa ophiolitic Belt (Eastern Cuba): Consequence of Interaction between volatile-rich
741 melts and peridotites in suprasubduction mantle. Economic Geology 94, 547-566.

742

743 Roberts, S., Neary, C.R., 1993. Petrogenesis of ophiolitic chromitite, in Prichard, H.M., Alabaster,
744 T., Harris, N.B.W., Neary, C.R., (Eds.), Magmatic processes and plate tectonics: Geological Society
745 of London, Special Publication 76, 257–272.

746

747 Rynearson, G.A., Smith, C.T., 1940. Chromite deposits in the Seiad Quadrangle Siskiyou county,
748 California: strategic minerals investigations. Bulletin 922-J, 281-306.

749

750 Tarkian, M., Naidenova, E., Zhelyaskova-Panayotova, M., 1991. PGM in chromitites from the
751 eastern Rhodope ultramafic complex, Bulgaria. Mineralogy and Petrology 44, 73-87.

752

753 Thayer, T.P., 1964. Principal features and origin podiform chromite deposits, and some observations
754 on the Guleman-Soridag district, Turkey. Economic Geology 59, 1497-1524.

755

756 Thayer, T.P., 1969. Gravity differentiation and magmatic re-emplacement of podiform chromite
757 Deposits, in: Wilson, H.D.B. (ed.) Magmatic Ore Deposits, Economic Geology Monograph 4, pp
758 132-146.

759

760 Tiller, W. A. 1991. The Science pf crystallisation: macroscopic phenomena and defect generation.
761 Cambridge University Press, UK.

762

763 Timms, N. E., Li, J., Reddy, S. M. 2009. Quantitative microstructural characterization of
764 natrojarosite scale formed during high-pressure acid leaching of lateritic nickel ore: American
765 Mineralogist 94, 1111–1119.
766
767 Uysal, I., Sadiklar, M. B., Tarkian, M., Karsli, O., Aydin, F., 2005. Mineralogy and composition
768 of the chromitites and their platinum-group minerals from Ortaca (Mugˇla-SW Turkey): evidence
769 for ophiolitic chromitite genesis. Mineralogy and Petrology 8, 219–242.
770
771 Van der Kaaden, G., 1970. Chromite-bearing ultramafic and related gabbroic rocks and their
772 relationship to "ophiolitic" extrusive basic rocks and diabases in Turkey. Geological Society of
773 South Africa Special Publication 1, 511-531.
774
775 Xu, X., Yang, J., Ba, D., Guo, G., Robinson, P.T., Li, J., 2011. Petrogenesis of the Kangjinla
776 peridotite in the Luobusa ophiolite, southern Tibet. Journal of Asian Earth Sciences 42, 553-568.
777
778 Zhou, M.-F., Malpas, J., Robinson, P.T., Sun, M., Li, J.-W., 2001. Crystallisation of podiform
779 chromites from silicate magmas and the formation of nodular textures. Resource Geology 5, 1-6.
780
781 Zhou, M.-F., Robinson, P. T., Malpas, J., Li, Z., 1996. Podiform chromitites in the Luobusa
782 ophiolite (SouthernTibet): Implications for Melt-Rock Interaction and Chromite Segregation in the Upper
783 Mantle. Journal of Petrology 37, 3-21.

Figure

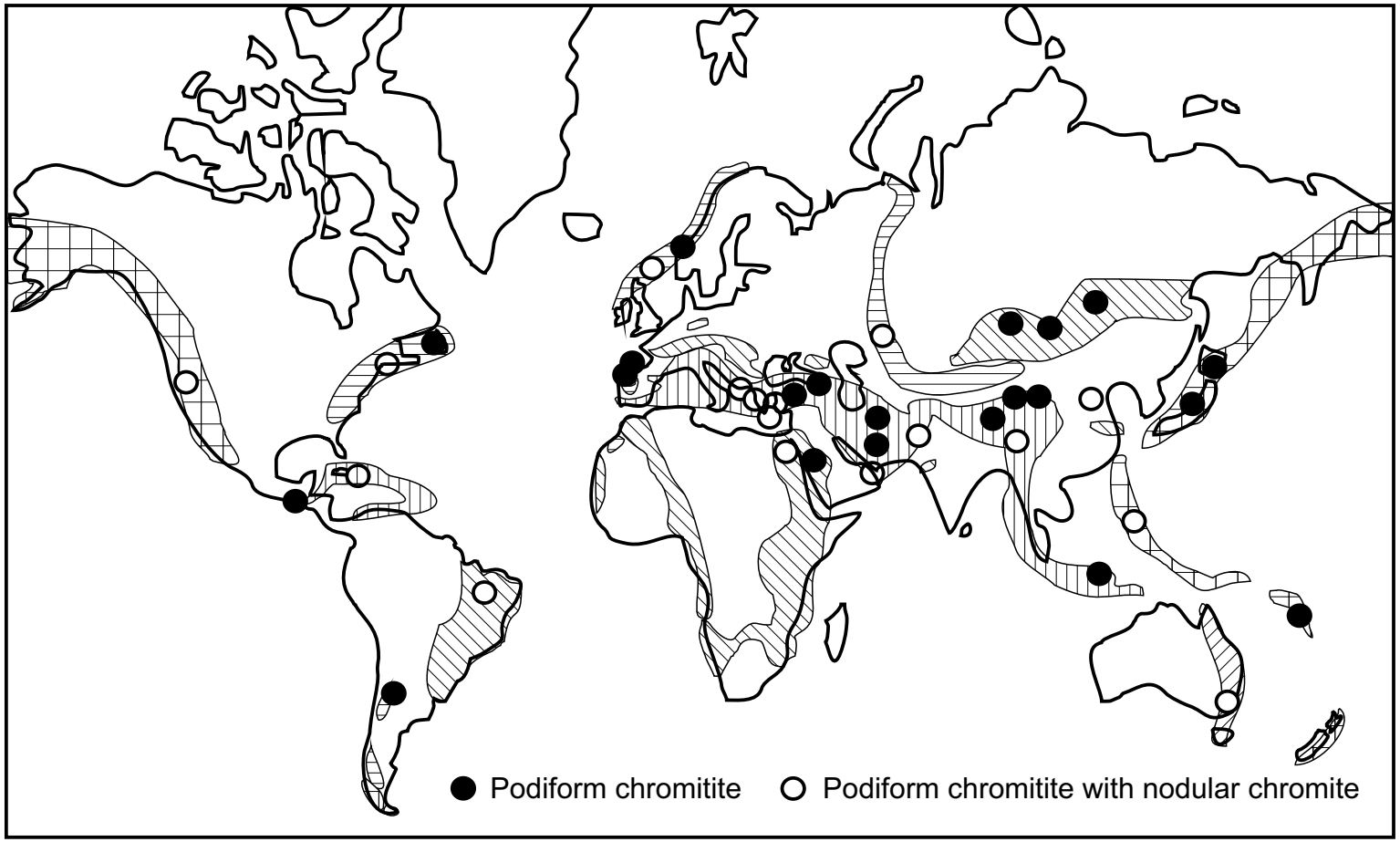
Podiform chromitite
Podiform chromitite with nodular chromite
(1) Pacific (Palaeozoic /Cenozoic)
(2) Tethyan/Carribean (Jurassic/Cretaceous)
(3) Appalachian/Caledonian/Hercynian (Paleozoic)
(4) Australian (Cambrian)
(5) Pan-African/Brazilian/Asian (Late Proterozoic)

Figure

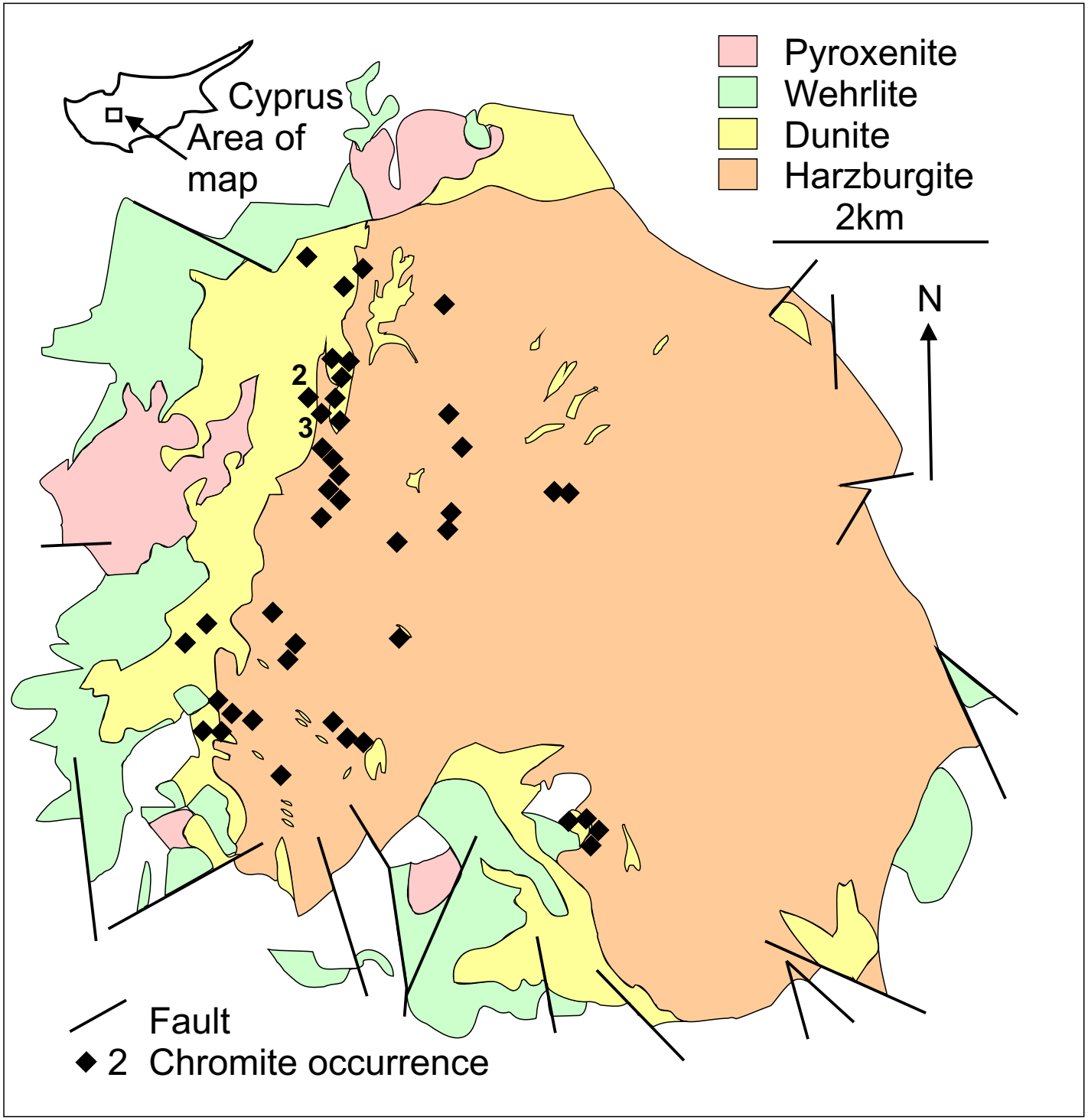
Cyprus
Area of
map
Pyroxenite
Wehrlite
Dunite
Harzburgite
2km
N
2
3
Fault
2 Chromite occurrence

Figure

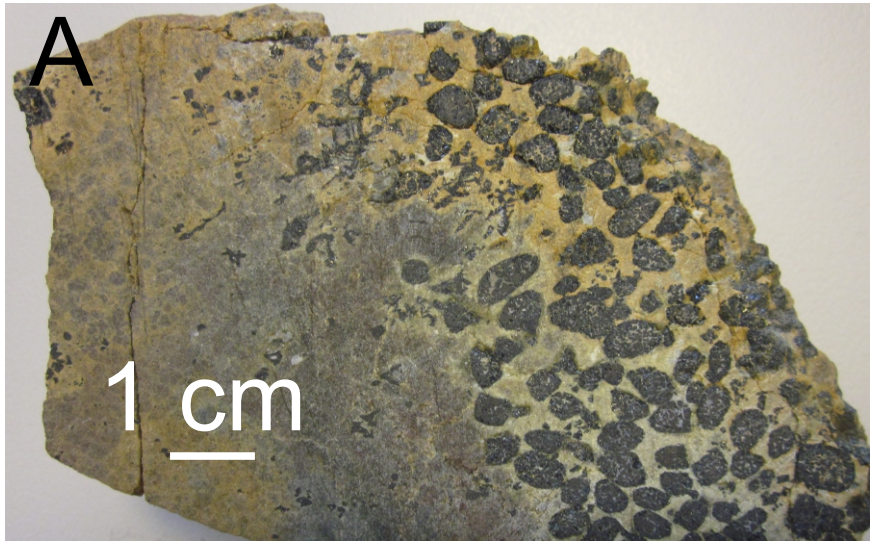

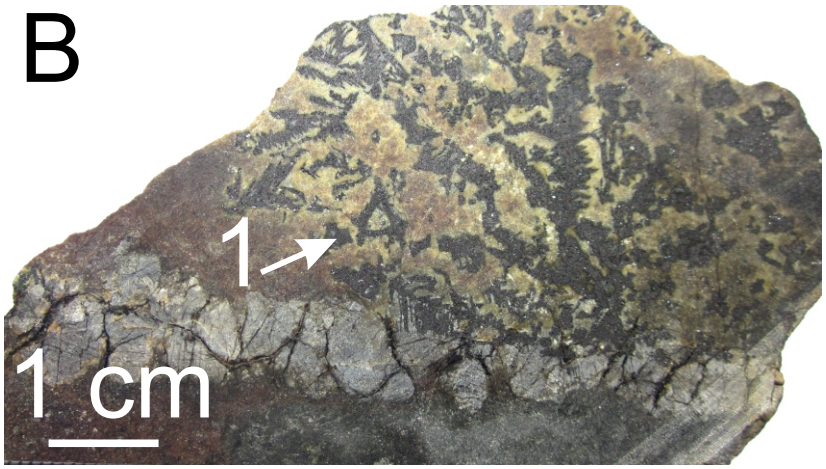

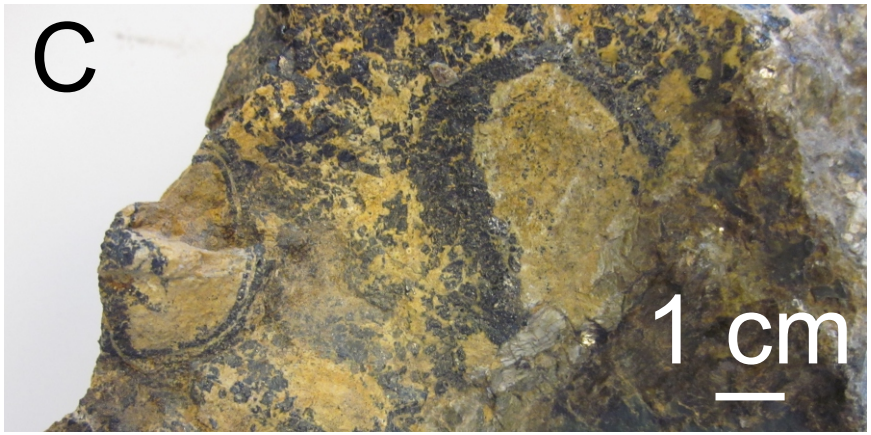

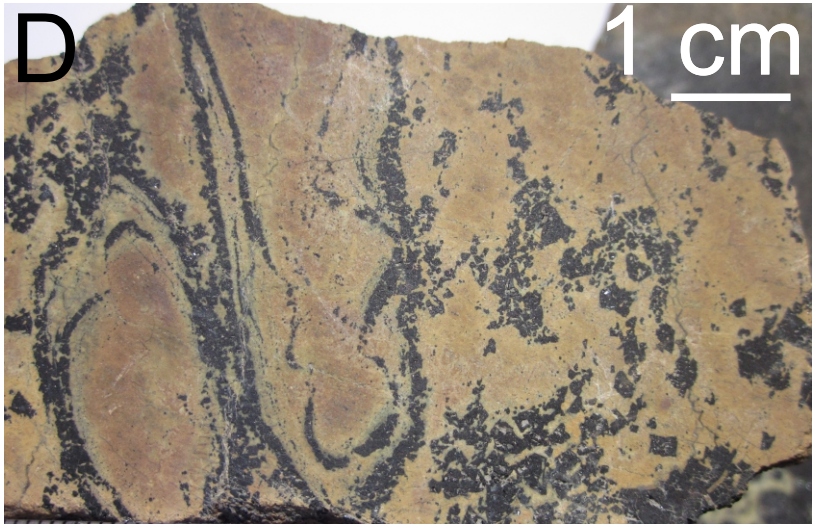

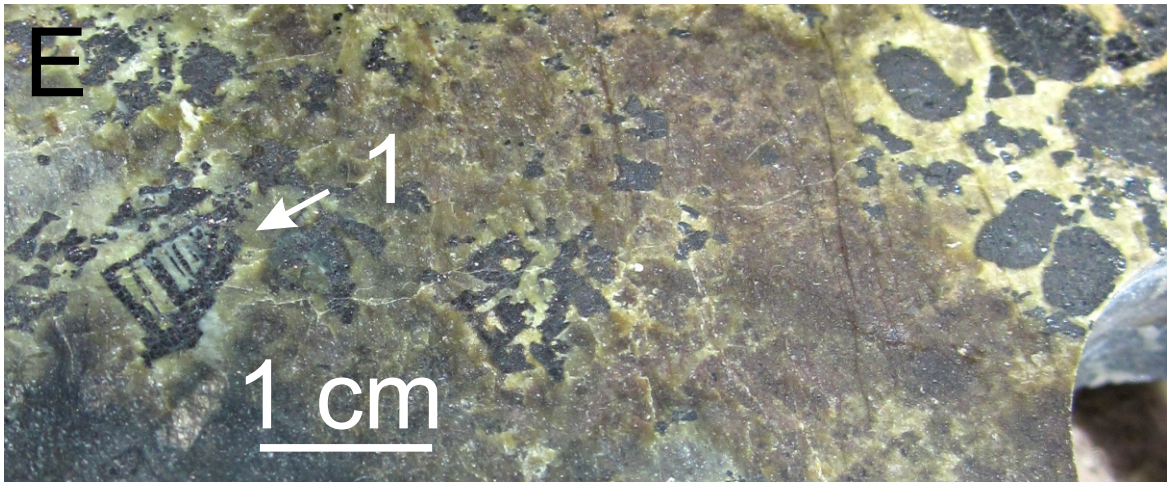

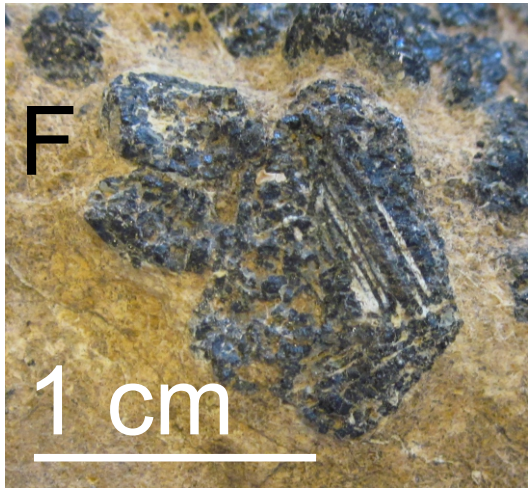

Figure

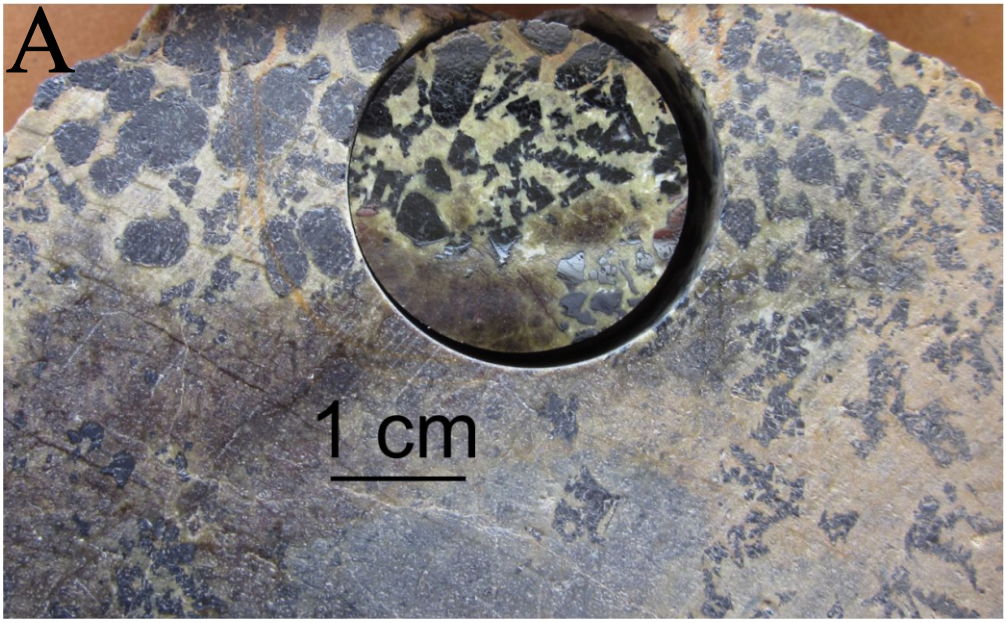

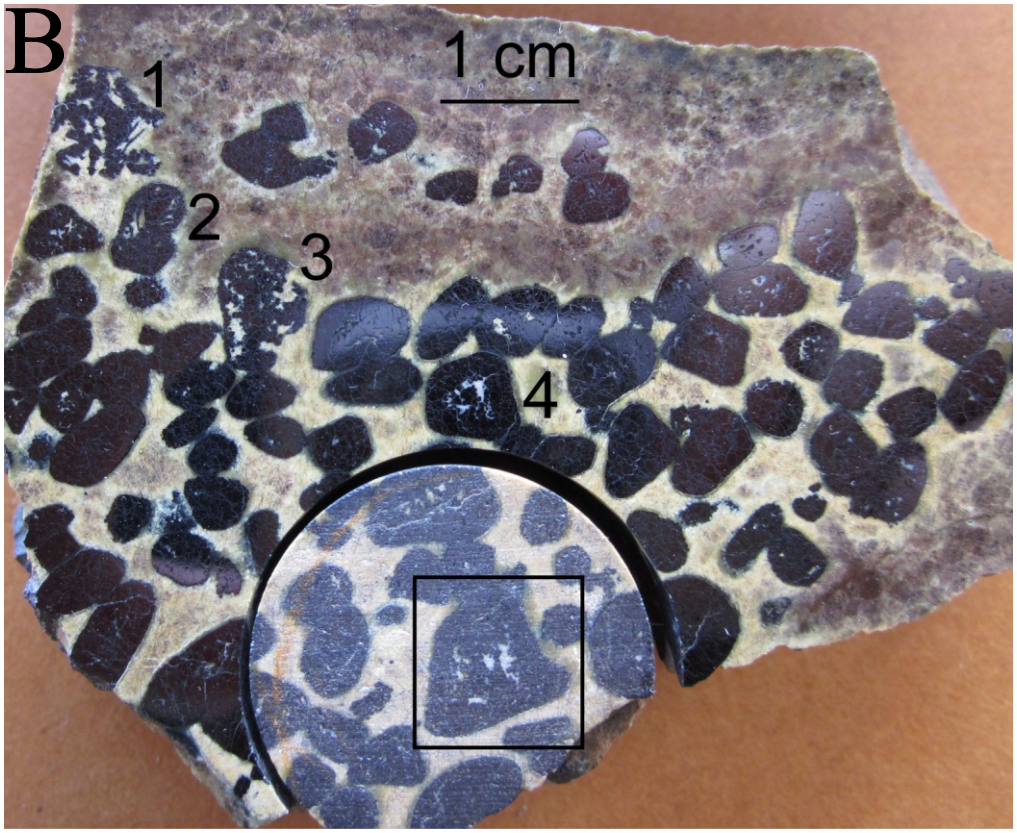

Figure

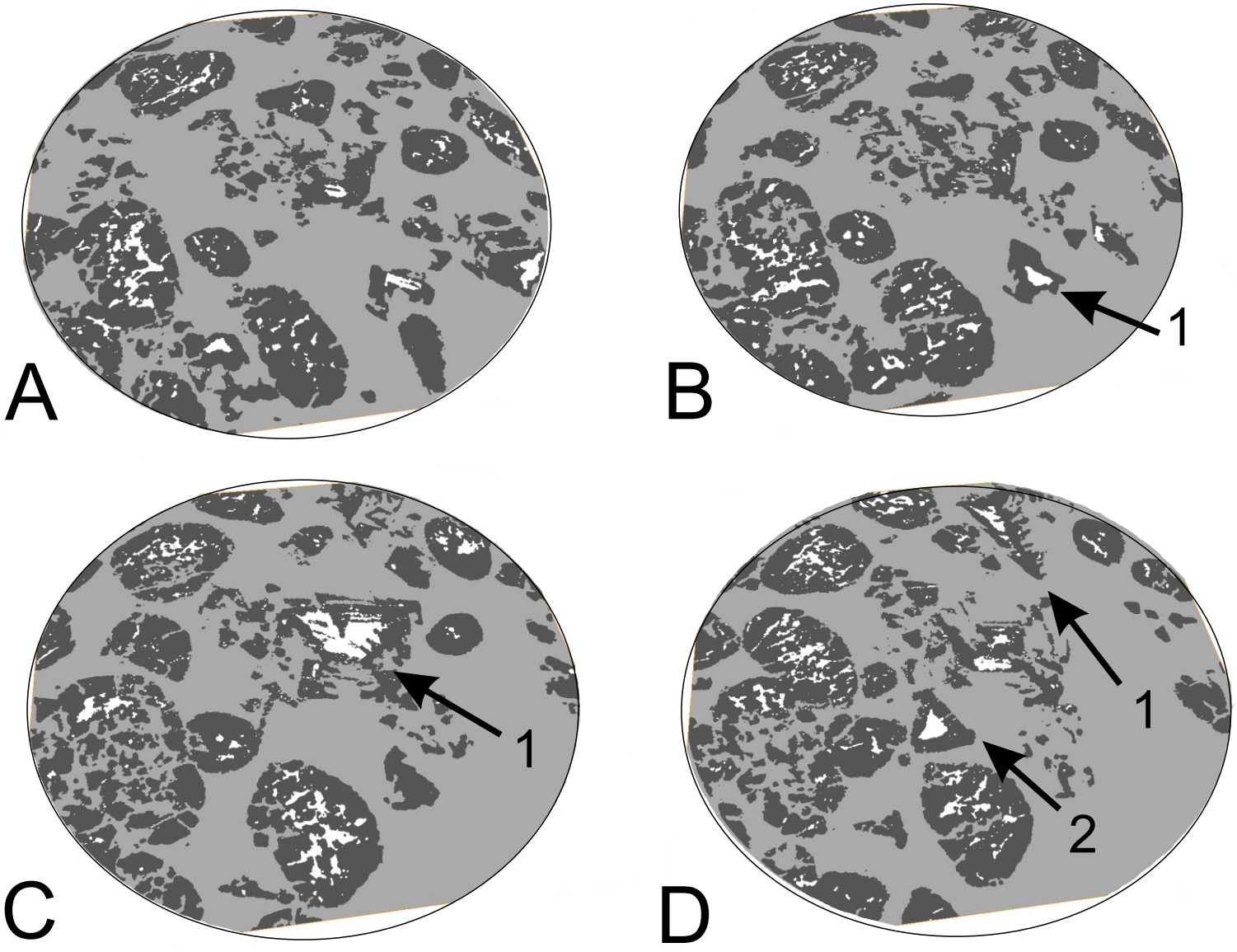

Figure

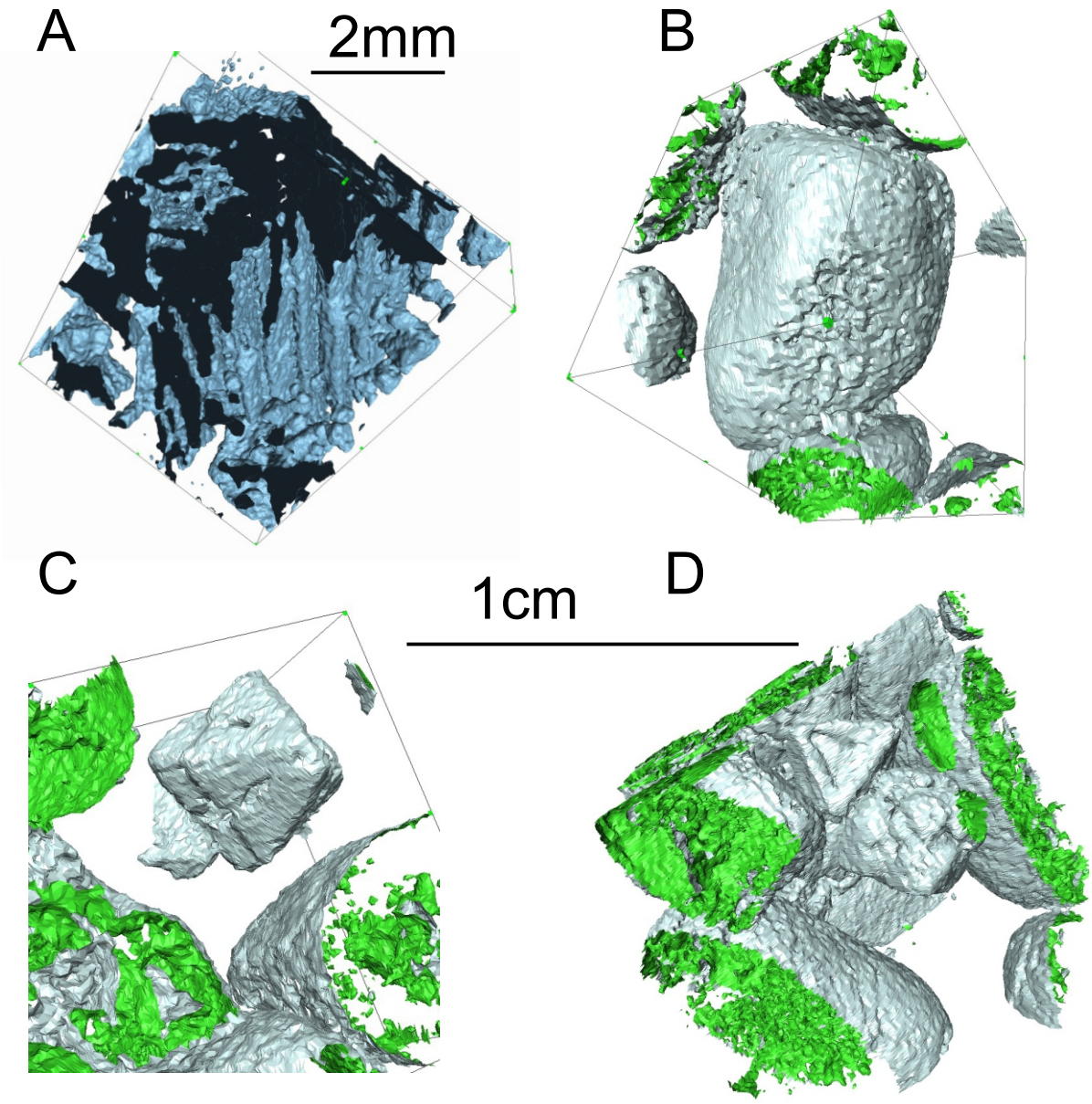

Figure

Fig. 7

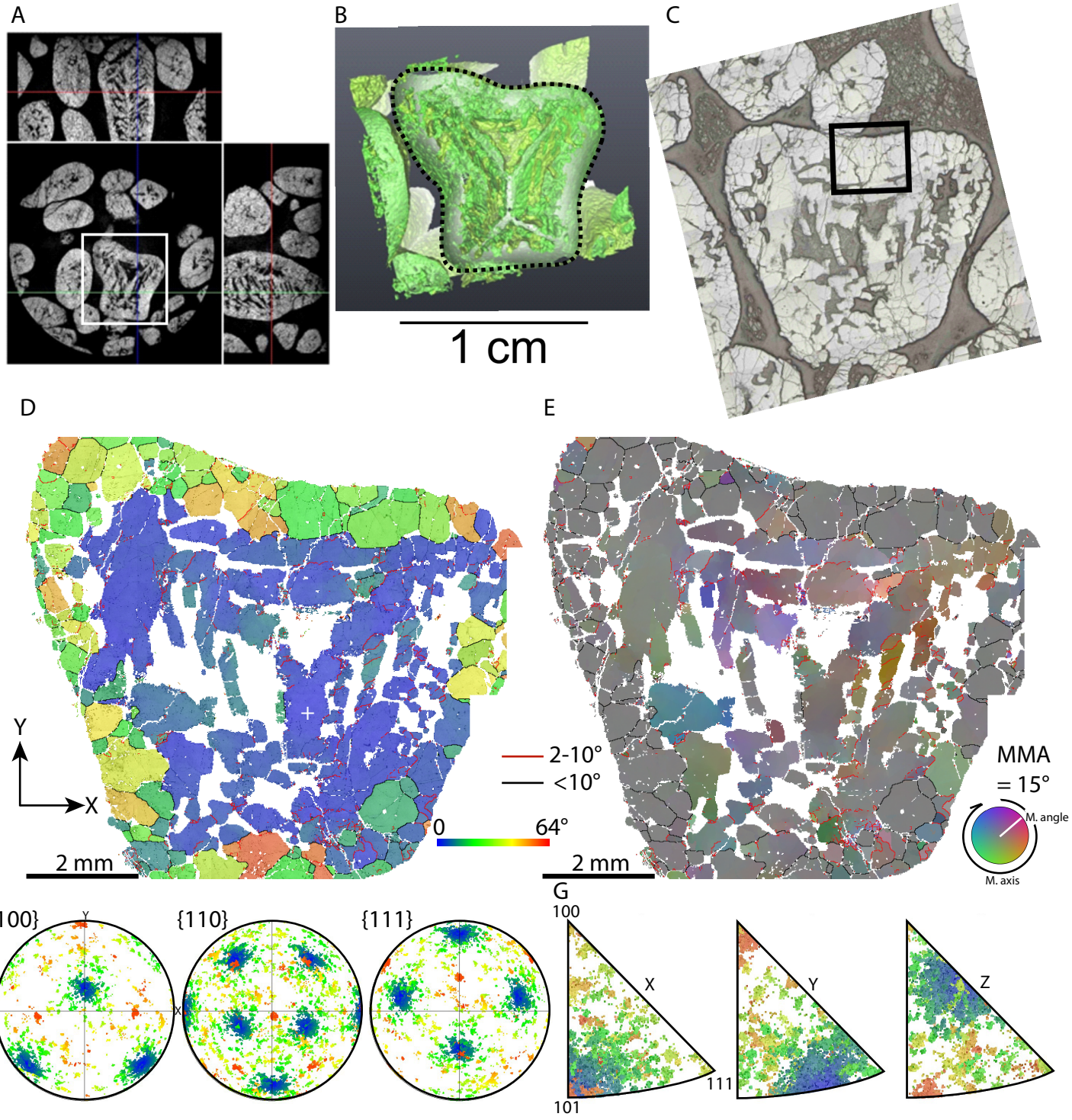
A
B
C
1 cm
D
E
Y
X
2 mm
2-10°
<10°
0
64°
MMA
= 15°
M. angle
M. axis
2 mm
F
{100}
{110}
{111}
G
100
X
Y
Z
111
101

Figure

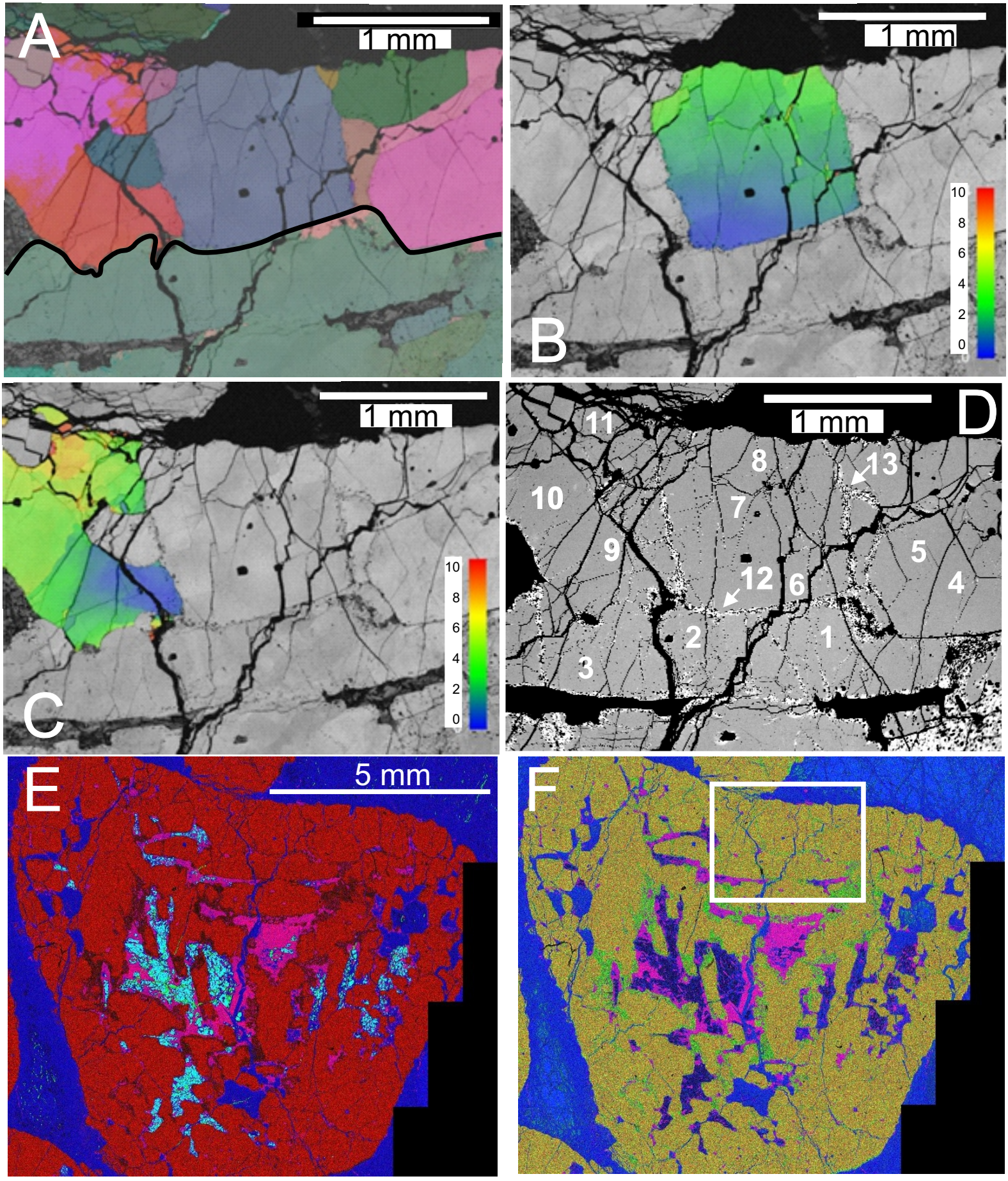
A
1 mm
B
1 mm
10
8
6
4
2
0
C
1 mm
10
8
6
4
2
0
D
1 mm
11
8
13
10
7
9
5
12
6
4
2
1
3
E
5 mm
F

Figure

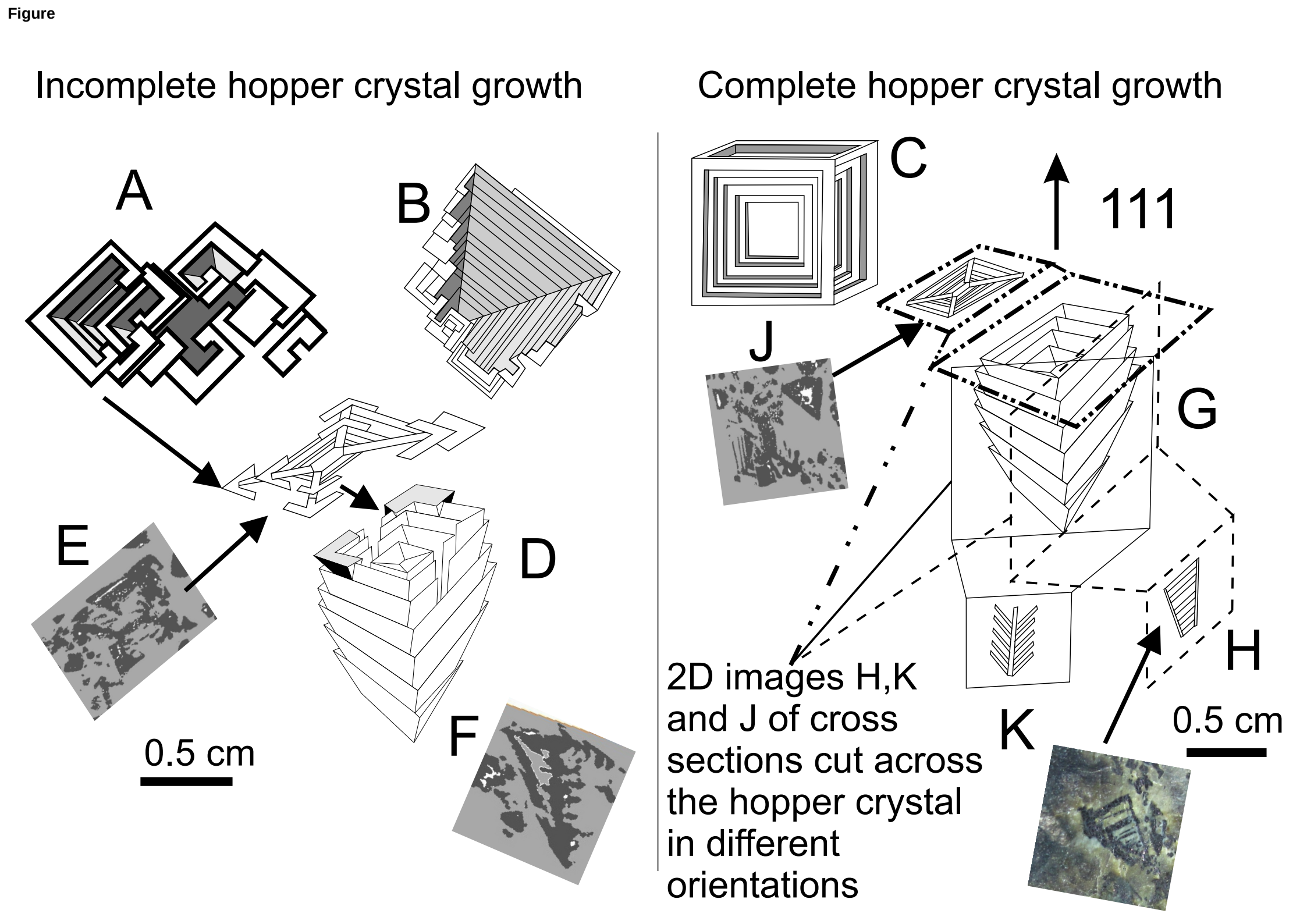
Incomplete hopper crystal growth
Complete hopper crystal growth
A
B
C
111
J
G
E
D
F
2D images H,K and J of cross sections cut across the hopper crystal in different orientations
K
H
0.5 cm
0.5 cm

Figure

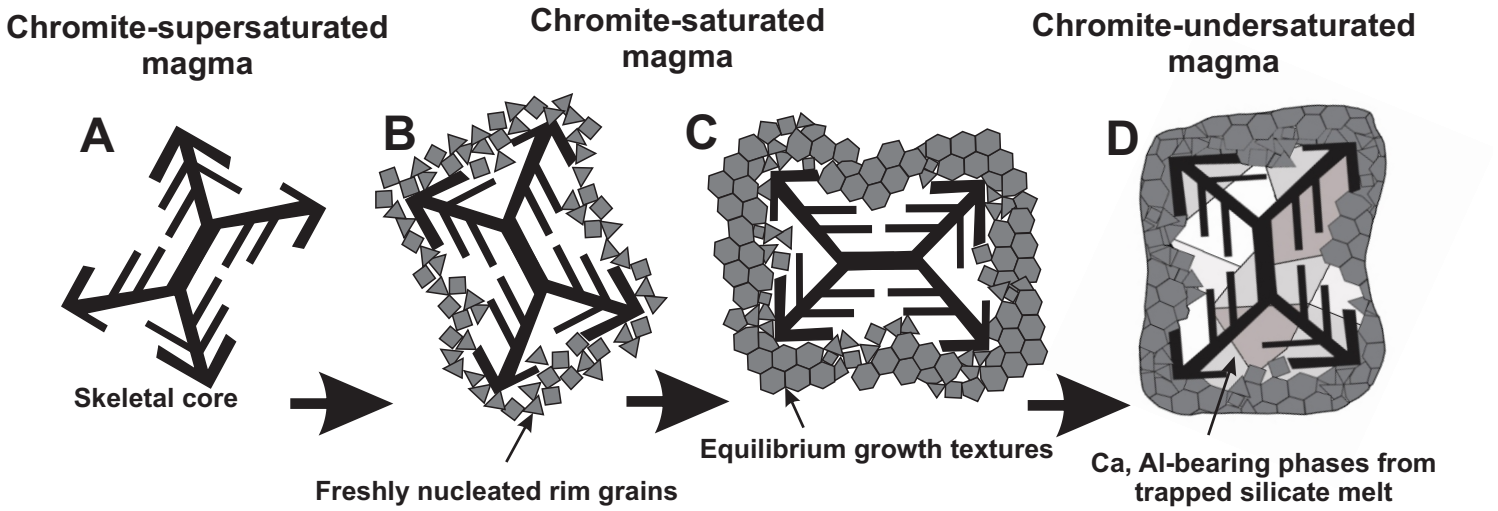
Chromite-supersaturated magma
Chromite-saturated magma
Chromite-undersaturated magma
A
B
C
D
Skeletal core
Freshly nucleated rim grains
Equilibrium growth textures
Ca, Al-bearing phases from trapped silicate melt

Figure

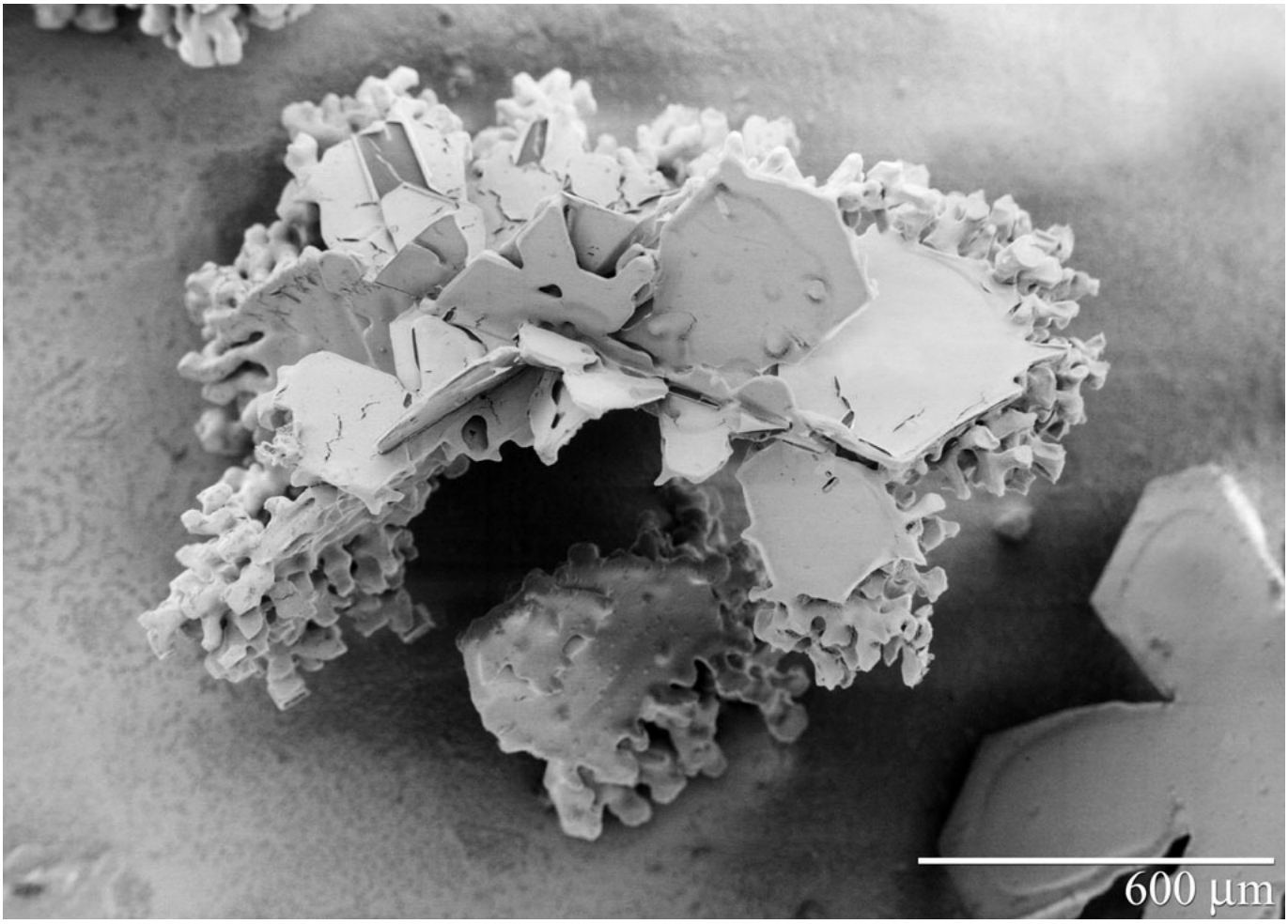

Table 1 Energy dispersive SEM analyses of chromite points shown in Fig. 8D

wt%	MgO	Al_2O_3	V_2O_5	Cr_2O_3	MnO	FeO	Fe_2O_3	Total	
1	12.79	12.57	0.22	56.85	0.52	17.1	0	100.04	Skeletal crystal
2	12.55	12.65	0.20	56.89	0.45	16.83	0	99.57	Skeletal crystal
3	12.76	12.58	0	57.17	0.65	17.24	0	100.39	Skeletal crystal
4	12.79	12.6	0	57.04	0.45	16.75	0	99.63	Grain in the rim
5	12.95	12.49	0.20	56.42	0.59	17.07	0	99.72	Grain in the rim
6	12.71	12.31	0.33	56.57	0	16.63	0	98.55	Grain in the rim
7	13.03	12.73	0.25	57.34	0.52	16.9	0	100.76	Grain in the rim
8	12.8	12.61	0	56.63	0	16.62	0	98.66	Grain in the rim
9	12.72	12.33	0.28	56.38	0.55	16.3	0	98.56	Grain in the rim
10	12.81	12.49	0.20	57	0.35	16.64	0	99.48	Grain in the rim
11	12.67	12.33	0.29	56.78	0.38	17.05	0	99.50	Grain in the rim
12	9.11	5.67	0	63.02	0.52	20.69	0	99.02	Altered grain rim
12	3.82	2.46	0	62.38	0.86	25.95	3.36	98.73	Altered grain rim
13	9.28	5.49	0	63.11	0.53	21.76	0	100.16	Altered grain rim
13	3.66	2.84	0	55.75	0.56	26.05	8.76	97.62	Altered grain rim